# BIMETALLIC GOLD AND PLATINUM NANOCATALYSTS IN WGS

by

**Yungchieh Lai**

Bachelor of Science, Chemical Engineering, National Taiwan University, 2008

Submitted to the Graduate Faculty of

Swanson School of Engineering in partial fulfillment

of the requirements for the degree of

Master of Science

University of Pittsburgh

2012

UNIVERSITY OF PITTSBURGH

SWANSON SCHOOL OF ENGINEERING

This thesis was presented

by

Yungchieh Lai

It was defended on

November 07, 2012

and approved by

Rongchao Jin, Ph.D., Associate Professor, Department of Chemistry

Lei Li, Ph.D., Assistant Professor, Department of Chemical and Petroleum Engineering

Thesis Advisor: Götz Veser, Ph.D., Professor, Department of Chemical and Petroleum Engineering

**BIMETALLIC GOLD AND PLATINUM NANOCATALYST IN WGS**

Yungchieh Lai, M.S.

University of Pittsburgh, 2012

The water gas shift (WGS) reaction plays an important role for hydrogen production from fossil and renewable resources. As an exothermal reaction, it is limited by thermodynamic equilibrium at high temperature and by slow kinetics at low temperatures. In order to achieve a high-equilibrium conversion and overcome slow kinetics, multifunctional catalysts for WGS have been widely studied. Au-based catalysts in particular have recently emerged as promising for low-temperature WGS, but the limited stability of Au is a major concern for technical application of these catalysts.

Cao and Veser recently demonstrated that alloying of metal particles can result in highly active nanocatalysts with exceptional high-temperature stability. In those studies, metals with essentially complete miscibility across the entire range of compositions were utilized. In the present study, we evaluated the extension of this principle onto catalysts with a wide miscibility gap by alloying Au nanoparticles with Pt. Both metals are known to show good WGS activity, but Pt has a much higher melting point and hence better thermal stability than Au.

AuPt bimetallic nanoparticles (NPs) were prepared by co-reducing polyvinylpyrrolidone (PVP) protected Au and Pt precursors with sodium borohydride in aqueous solution. Despite the wide miscibility gap between the two (bulk) metals, we were able to form well-controlled, homogeneous bimetallic NPs over a broad range. The as-synthesized NPs were then deposited onto ceria and silica as supports. The materials were characterized using a range of techniques,

including XRD, TEM, HRTEM, and UV-Vis, and then evaluated with regard to thermal stability during calcination in air. We found that the bimetallic nanoparticles spread on the two supports exhibit different phase behaviors during heat treatments, albeit they all suffer partial or complete phase segregations. While AuPt/$SiO_2$ phase-separates into the thermodynamically stable Au-rich and Pt-rich phases already at T>400℃ and become a Pt-core/Au-shell structure, the bimetallic nanoparticles deposited on ceria undergoes a complete phase segregation into separate Au and Pt-rich nanoparticles during heat treatments, and only fused to form the thermodynamically stable phases at T ~900℃. Clearly, metal-support interactions strongly dominate the behavior of this bimetallic system. Fixed-bed reactor and the TPD experiments further demonstrate that the WGS activity of these catalysts strongly correlate with the phase stability of the bimetallic nanoparticles. Overall, our results demonstrate that, while previously suggested principle of catalyst stabilization via alloying with a higher melting-point component may hold even for systems with a miscibility gap, metal-support interactions are critical in the consideration of materials stability and can even dictate catalyst stability.

## TABLE OF CONTENTS

## LIST OF TABLES

## LIST OF FIGURES

## ACKNOWLEDGEMENTS

I would like to thank Dr. Götz Veser for his assistance in completing my thesis and for stepping in as my thesis advisor. I really appreciate everything you have done for me. I would like to thank Dr. Shuang Liang for his guidance and direction.

I would like to dedicate this to my father and mother, for shaping me into the person who I am today and support my study here. Thank you to my brothers and the rest of my family for all their support and guidance through these years. Finally, thank you to my girlfriend, Yaran Cheng, who stayed with me and encouraged me all the time in these two years. You have all made valuable additions to my education over the years. Thank you all.

# 1.0 INTRODUCTION

## 1.1 WATER-GAS SHIFT (WGS) REACTION

The water gas shift (WGS) reaction was first reported by Mond and Langer in 1888 [1].

$$CO\ (g) + H_2O\ (g) \Leftrightarrow CO_2\ (g) + H_2\ (g)\ (\Delta H = -41.1\ KJ / mol) \quad (1)$$

It was regarded as one of the most important industrial catalytic reactions in 1915 when the first coal- based ammonia synthesis plant was built [2]. WGS is popular also due to other coal-based processes which require a proper $CO/H_2$ ratio in syngas to produce methanol and hydrocarbons, for instance, Fischer-Tropsch process.

Recently, the increase use of hydrogen in transportation and electricity generation such as fuel cells [3, 4], whose increased thermal efficiency and reduced environment impact compared to conventional energy is significant. Consequently, there are several processes developed for hydrogen production; among them, steam reforming is the one mostly considered because it can provide the highest molar ratio of $H_2/CO$ of 3.

$$CH_4 + H_2O \Leftrightarrow CO + 3H_2\ (H_2/CO = 3;\ \Delta H = 206.3\ KJ / mol) \quad (2)$$

However, these coal-derived syngases where CO concentration is still relatively high (40-60%) [5], and could poison catalysts used downstream. WGS hence attracts great attentions to adjust the CO to hydrogen ratio and/or to provide clean hydrogen.

There are three general types of catalysts as well as a more recently studied precious metal- based nano-catalysts for WGS. In traditional industry, the first type is of high temperature shift (HTS) catalyst, which is typically the promoted iron oxide (e.g. by Chromium) and is used at the temperature ranging between 350- 450℃. Another one is copper-zinc oxide, which is a low temperature shift (LTS) catalyst and usually used at 190-250℃. WGS is mildly exothermic and thermodynamically limited at high temperatures. High conversions are favored at low temperature and conversion is not affected by the changes in total pressure [6]. Accordingly, current industry designs a two-stage process involving the above HTS and LTS catalysts in a series to achieve a high-equilibrium conversion and overcome low kinetics. Sulfur poisoning on catalysts is another concern in WGS and is significant even the extremely low concentration of S can cause complete deactivation and shut down the reaction (e.g. HTS Copper catalysts). Therefore, the third type called sulfur-resistant catalyst has been extensively explored, and they are typically cobalt and molybdenum sulfides.

Nonetheless, these three types of WGS catalysts suffer from several disadvantages. Due to the relative low reactivity of these catalysts and low space velocities, especially for the LTS step (GHSV= 3000-5000 $h^{-1}$ for LTS and 10000-15000 $h^{-1}$ for HTS) [7] and Co-Mo catalysts, large catalyst bed volume and more catalysts are required [8]. The toxic and environmentally-unfriendly $Cr^{+6}$ in HTS catalyst as well as the Cu-based LTS catalyst which requires careful activation (i.e. due to its pyrophoricity) are other severe concerns. Moreover, molybdenum-based catalysts are active only in the sulfide form. To use this kind of sulfur-resistant catalyst for WGS, the inlet sulfur should be maintained at a certain concentration to keep their activity. All these issues force the emerging technologies such as carbonate fuel cell (MCFC) and solid oxide fuel cell (SOFC) systems to look for a new catalyst to meet the requirements of WGS

applications. Recently, the oxide-supported precious metal WGS nanocatalysts are developed to be operated over a broad temperature range [9].

Unfortunately, the reaction path over oxide supported metal catalysts is still under debate. Two main pathways have been postulated. The first one is associated with a support-mediated surface redox process [10]. The absorbed CO on the metal reacts with oxide support to generate $CO_2$, and the support is then replenished with oxygen by $H_2O$. This is known as the redox mechanism. The alternate pathway which proceeds via a surface formate [11] is referred to as an associative mechanism. In this mechanism, surface dissociated OH group are believed to react with absorbed CO to form a surface formate intermediate, and $CO_2$ and $H_2$ are then produced from the decomposition of surface formate. Despite of the differences, the interface between the CO bonding metal phase and the oxygen supplying support play an important role in both hypotheses in WGS, serving as the active sites for the oxidative half step.

## 1.2 ACTIVE METALS

Among oxide-supported metal nanocatalysts, Au and Pt as active metals were intensively studied. The particle size of both was all agreed to be less than 5nm in nanoscale to be active in WGS, and they are discussed as below respectively.

### 1.2.1 Gold

Metal oxide supported nanoscale Au has been shown to be active for many reactions [12] since the discovery of gold's surprising high catalytic activity for low temperature CO oxidation [13].

More recently, it is extensively studied in WGS [14]. Previous studies indicate that gold nanoparticles finely dispersed (2-5 nm) on reducible supports such as α-$Fe_2O_3$, $TiO_2$ and $ZrO_2$ manifest high-catalytic activity in the low-temperature WGS reaction [15-17]. Stephanopoulos's group reported that Au on nanostructured ceria is another excellent choice for WGS where the reducibility of the ceria support has great influences on the catalytic activity [18]. Sandoval et. al. compared both reducible ($TiO_2$ and $CeO_2$) and non-reducible ($Al_2O_3$ and $SiO_2$) supports for low-temperature WGS [19]. The activity of Au on reducible supports was shown to be much higher than that on non-reducible ones, and the $Au/SiO_2$ catalyst was practically inactive. The interaction between gold and supports can hence be concluded to be an important consideration responsible for its catalytic activity.

In addition, since bulk gold is known to be catalytically inert, the particle size of gold is an important factor for its activity in a reaction. The nanoscale gold size is known to be highly sensitive to the preparation technique, Haruta hence has developed four synthesis techniques (i.e. co-precipitation (CP), co-sputtering, deposition-precipitation (DP) and gas-phase grafting) to acquire small nanoparticles on specified metal oxides: [20]. For example, T. Tabakova et. al used a modified DP method to produce gold/ceria catalysts, with the original method giving a much smaller gold particle size on the support. The smaller size gold thus shows a significant higher catalytic activity in low temperature WGS because of the higher amounts of active gold sites in close contact with oxygen-vacancy defects of ceria at the surface. [21]

Nonetheless, thanks to the intensive development of synthesis of gold catalysts in the past decades, the particle size nowdays can generally be controlled well, even down to atomic dispersion on some supports. Another concern affecting particle size is the thermal stability of

gold. Thermal instability sets on below the melting point, and an equation for the size dependence of melting point ($T_m(r)$) on particle radius (r) was derived by Buffat and Borel [22]:

$$\frac{T_m(r)}{T_m(0)} = 1 - \frac{2}{\rho_s L}\left\{\gamma_s - \gamma_l\left(\frac{\rho_s}{\rho_l}\right)^{\frac{2}{3}}\right\}\frac{1}{\gamma_s}$$

Where $\rho$ and $\gamma$ are density and surface free energy of the solid (s) and liquid (l), L the molar heat of fusion, and $T_m(0)$ the bulk melting point, respectively. For example, the melting point of bulk gold is around 1300 K, but it drops dramatically as the particle size gets smaller (Figure 1) [23]. The higher mobility of the smaller particle size of gold would then increase the tendency of particle agglomeration and consequently limits its applications in high temperature reactions. More efforts should be done to enhance the thermal stability of gold to maintain the particle size and enhance it's reactivity.

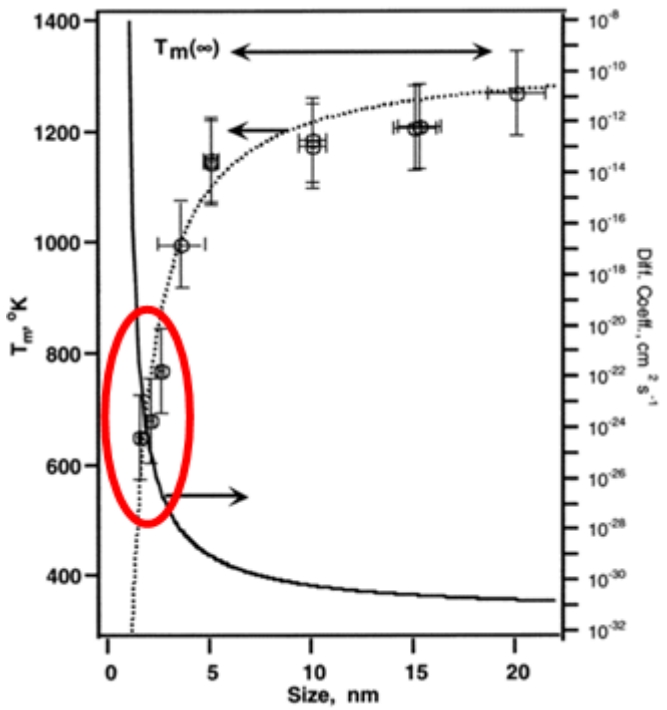


**Figure 1.** Size dependence of the melting point and diffusion coefficient of silica-encapsulated gold particles. The dotted curve is calculated using eq1. The bulk melting temperature of Au is indicated by the double arrow as $T_m(\infty)$. The solid curve (right-hand side axis) is the calculated Au self-diffusion coefficient [23]

### 1.2.2 Platinum

Compared to the high activity of gold in low- temperature WGS, Pt was shown to behave more stable and to perform better than Au for WGS reaction at high temperature [24]. However, due to the high activation energy for typical Pt catalysts, its activity at low temperature is generally lower than that of Au catalysts. Therefore, enhancing the reactivity of Pt at lower temperature is extensively studied, where tailoring the oxide support and using metal promoter especially attract great attentions.

Similar to Au-based WGS catalysts, the oxide support of Pt-based catalysts is found to adsorb and activate water due to the thermodynamic instability of PtOx species under WGS environment. A number of reducible substrates were already evaluated for WGS, for example, $CeO_2$, $ZrO_2$, and $TiO_2$. Moreover, the surface properties of a metal oxide may be further improved with the incorporation of another metal oxide. For example, Pt supported by $CeO_2$–$ZrO_2$ was found to be very active for both HTS and LTS, and much better than other noble metals as this composite support was used [25]. Cerium- modified $TiO_2$ for Pt, reported by González et. al, was demonstrated to be not only more stable but also more active than individual ceria and $TiO_2$ [26]. They explained this based on the catalytic properties of the redox pair $Ce^{3+}/Ce^{4+}$ which can replace $Ti^{4+}$ ions to improve the thermal resistance to sintering and redox properties of $TiO_2$. Tailoring supports with metal promotion is another way to enhance the platinum catalysts. A series of platinum catalysts supported on cation (Me)-doped cerium oxide (Me = Ca, La, Mg, Zn, Zr, Yb, Y, Gd) was prepared by Panagiotopoulou [27]. The promotion effect was shown to influence the reducibility and lattice oxygen mobility of the $CeO_2$ support, which consequently change the WGS activity of dispersed platinum crystallites.

Beyond the metal promotion studies, alkali promotion of Pt results in excellent WGS, and, more importantly, the support is not limited to the reducible ones anymore. This is confirmed by Stephanopoulos' group via kinetic studies from which yield similar activation energies for all alkali-stabilized catalysts with irreducible supports, with a value that is close to Pt- based catalysts supported on reducible support such as $Pt/CeO_2$, $Pt/TiO_2$ and $Pt/ZrO_2$ ($E_{act}$ = 70±5 kJ/mol). This suggests that the active site is identical between these catalysts, and that the difference in reaction rates can be attributed to the different number of active sites ($Pt\text{-}OH_x$). These findings are useful for the design of highly active and stable WGS catalysts which require only little mount of platinum without need for a reducible support [28].

## 1.3 OXIDE SUPPORTS

The nature of the support on which precious metal- based nanoparticles are dispersed (i.e. Gold-metal oxide interface) plays a crucial role in determining the catalytic activity and catalytic capabilities. Although the role varies from stabilizing an active metal to acting as electron/acceptor, and eventually being an quasi-independent co-catalyst for part of the overall reaction by supplying oxygen for CO oxidation and/or directly catalyzing the reduction of water [9], reducible oxide generally makes the precious- metal based catalysts more active than the irreducible oxide supported ones. For instance, noble metals (Pt and Ru) on irreducible supports such as $SiO_2$ and $Al_2O_3$ are 1–2 orders of magnitude less active in WGS compared to catalysts supported on reducible metal oxides [29].

### 1.3.1 Cerium oxide

$CeO_2$ has been shown to be as one of the most effective and active supports for low temperature catalysts in the last decade. The facile conversion between $Ce^{+4}$ and $Ce^{+3}$ on the oxide surface allowing cerium oxide to act as oxygen storage and oxygen transfer material in redox reactions is the main reason that makes $CeO_2$ attractive, despite of the fact that the role played by $CeO_2$ is still a matter of debate [18].

An increase in defect density can be achieved by decreasing particle size to create more active redox sites (i.e. oxygen vacancies) [30]. It has been also shown that the reducibility of ceria is structure sensitive due to the observation of much stronger binding of CO on the surfaces of rods and cubes [31, 32]. The lattice oxygen on ceria rods was also determined to have the highest mobility [33], the sequence of reducibility is thus to be rod > cube > polyhedral. More recently, Si et al. compared various nanostructured ceria catalysts in WGS and found that ceria nanorod supported Au shows better reactivity than any other nanostructure-based catalysts [34]. ; Beyond the morphological tailoring studies of ceria, modifying the support properties with doping impurities is also extensively studied like illustrated before. For example, Liang et. al. successfully synthesized lanthanide doped ceria in a homogeneous phase and demonstrated a 25% of lanthanide content results in a maximum reducibility [35]. They further indicate that the reactivity of lanthanum doped cerium oxide supported Au does correlate closely with the reducibility of the composite oxide support.

However, most of ceria supported precious metal are not sufficiently stable and gradually deactivate under conditions typical of a reformer outlet [36]. This can be attributed to several factors in addition to sintering of supported active metals, including irreversible reduction of the

support, deforming of well-defined nanostructures at higher temperature, and carbon deposition or formation of cerium hydroxycarbonate species [37].

## 1.4 ENHANCEMENT OF THERMAL STABILITY

The deactivation due to sintering (i.e. agglomeration of metal nanoparticles) is a major concern. Accordingly, strategies used to maintain reactivity of precious metals have been extensively researched. Recent progress in this area has focused on nanostructured oxides to stabilize embedded metal nanoparticles (NPs) [38-40], including encapsulation and caging the metal nanoparticles in a nanostructured support. Cargnello and coworkers corroborate this concept by comparing Pd/ceria synthesized by normal impregnation with Pd-core/ ceria-shell. The core-shell catalysts did exhibit better stability in high temperature WGS, however, the low Pd accessibility results in overall poor activity. To overcome this problem, Pablo et. al successfully synthesized gold nanoparticles encapsulated on the inside of the hollow zirconia sphere. The thin and porous zirconia shell avoids mass transfer limitations, results in a better activity [38]. Alternatively, metal nanoparticles encapsulated by a silica layer via atomic layer deposition (ALD) were synthesized by Ma et. al [39]. In spite of a significant sintering resistance, low catalytic activity is still inevitable. So far, no efficient nanostructured oxide to stabilize particles to be below 5nm (i.e. very active for WGS) at high temperature environment has been demonstrated.

A state of the art approach to obtain improved high-temperature stability by synthesizing bimetallic NPs was reported by Cao and Veser recently [41]. In this technique, the low melting Pt is stabilized by more stable Rh via alloying. As the temperature increased for PtRh bimetallic NPs, low-melting point Pt bleeds out and the Rh contents in the remaining NPs increase

accordingly. This ‘distillation’ of Pt from PtRh NPs results in a sacrificial self-stabilization of the bimetallic NPs. Hence the catalyst with sufficient ratio of Rh/Pt shows an excellent stability in the reactions to as high as 850℃. This approach has also been shown to be efficient in several miscible bimetallic systems.

## 1.5 BIMETALLIC GOLD AND PLATINUM NANOPARTICLES

AuPt bimetallic system is a bimetallic system which has recently been intensively studied due to the synergistic effect of Au and Pt in many reactions. In addition, stability based on phase properties of bimetallic NPs play an important role for applications as a catalyst, and it is hence critical to have a good understanding of it. An overview of bimetallic AuPt NPs is thus discussed below.

### 1.5.1 Bimetallic structures

Phase structure of bimetallic catalysts is a big concern for their applications. Generally, the structure of bimetallic nanoparticles (NPs) can be divided into four categories; core/shell, heteroaggregate (dendritic structure), partially segregated alloy, as well as pure alloy (Figure 2).

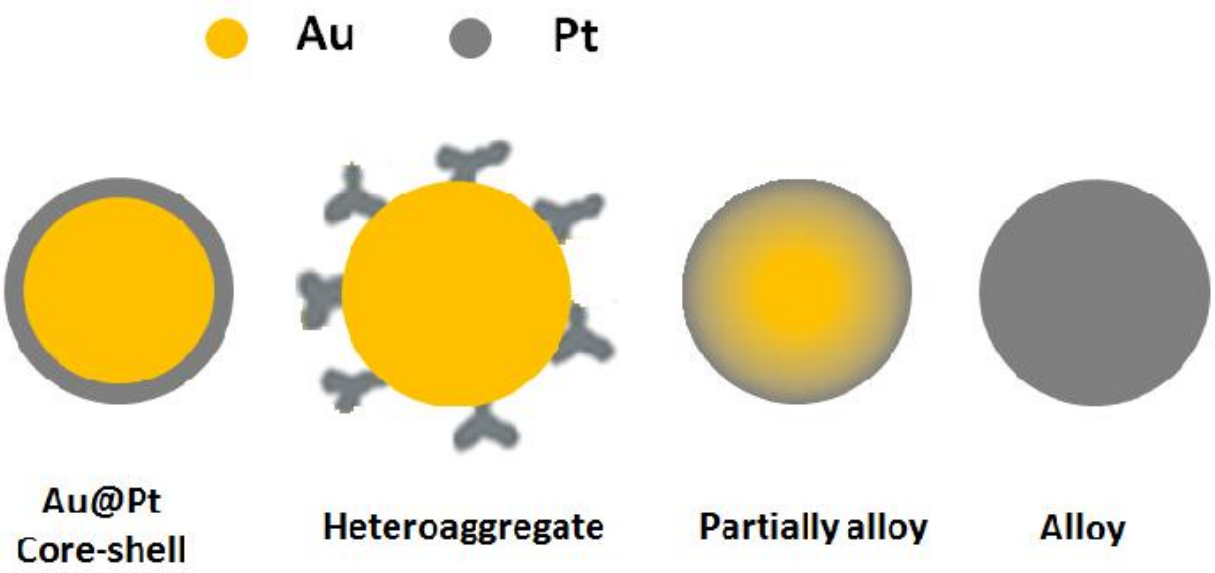


**Figure 2.** Possible architectures in bimetallic systems. Adapted from [47]

Common techniques used for analyzing bimetallic NPs are UV/vis spectroscopy, x-ray diffraction (XRD), energy dispersive x-ray (EDX) analysis, and high resolution transmission electron microscopy (HRTEM). Vegard's law which holds that a linear relation exists between the crystal lattice parameter of an alloy and the concentrations of the constituent elements at constant temperature is an usefully empirical rule for examining bimetallic alloy. The linear relation for bimetallic AuPt alloy is illustrated in Figure 3 [42, 43].

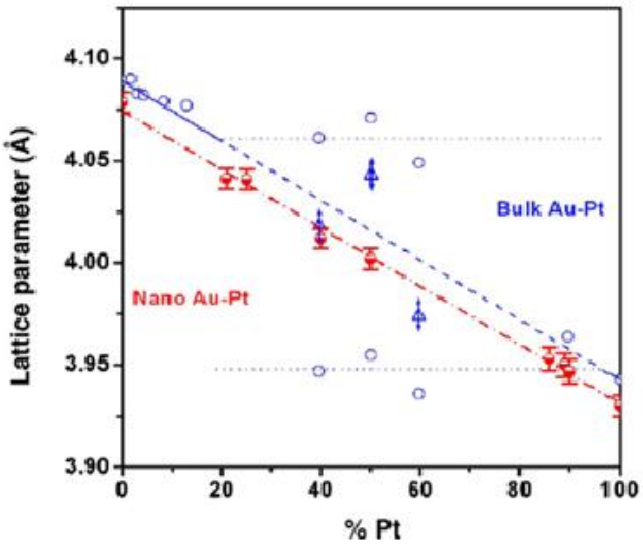


**Figure 3.** The lattice parameters vs. Pt% for AuPt NPs ( ), bulk ( ) (triangle points represent a frozen state for bulk metals) [46]

### 1.5.2 Chemical reduction synthesis

Methods and processes for synthesizing bimetallic NPs are similar to those for pure monometallic clusters, such as chemical reduction (co-reduction or successive reduction for different structures desired), thermal decomposition, electrochemical synthesis or radiolysis. Among them, chemical reduction was most investigated due to its simplicity and easy accessibility. However, gold-platinum alloys are relatively difficult to prepare by chemical reduction method because of the different rates of reduction. Therefore, gradient alloy or complete phase segregation happened for most of cases. For example, Chen et. al prepared Au/Pt bimetallic NPs in water-in-oil microemulsion [44] via a fusion-redispersion process to exchange contents. The bimetallic structure they acquired was a gradient alloy, because faster nucleation rate of Au forms a higher Au content in the core followed by deposition of Pt on the Au enriched core.

In terms of pure AuPt alloy, in 1998, Zhong et.al [45] came up with a two phase synthesis method called monolayer-protected alloy clusters with many advantages. In principle, the approach was carried out by dissolving metal precursors in toluene/water biphasic solution, and then reducing the metal precursors with sodium borohydride in presence phase transfer reagents. In this synthesis, the alkanethiolate monolayer is the key to prevent the metal aggregation and the product is able to be obtained in consistently high yield. The alloyed NPs can be not only isolated in solvent free forms but also re-dissolved in solvent without any changes. Furthermore, the core composition can be varied by adjusting the feed ratios and numbers of groups 10 and 11 metals. They later utilized a modified two phase method which successfully synthesized even smaller size Au/Pt nanoparticles with 2 nm, which were then deposited on carbon black by impregnation (Figure 4). The following thermal treatments were used to make the catalyst crystalline and remove the capping reagents.

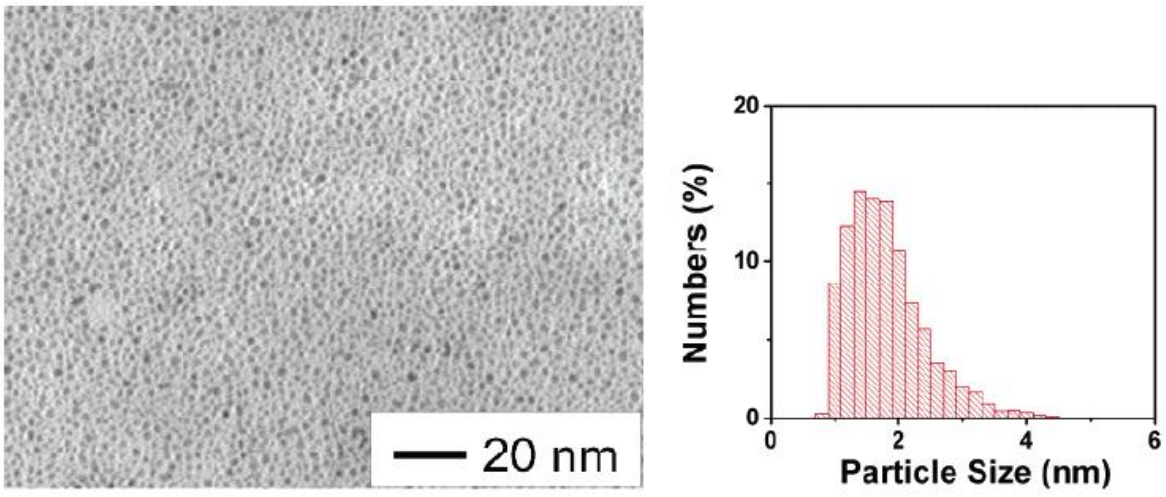


**Figure 4.** TEM images and particle size distribution for $Au_{82}Pt_{16}$ NPs [46]

Zhou's group then employed an one-pot synthesis without post-annealing to make AuPt alloy by using a rapid butyllithium reduction of $Au^{+3}$ and $Pt^{+4}$ [47]. With this method, they successfully obtained alloys for both sphere and rod shape by adjusting the amount of reducing

agent as well as synthetic conditions. They further showed that a rapid reduction is the key point to get AuPt alloy NPs, and this is the first non-templated synthesis approach of 1D AuPt alloy nanorods.

Beside the two-phase synthesis, Zhong also reported the synthesis of AuPt bimetallic alloy in aqueous solution [48]. In their route, the bimetallic AuPt alloy was acquired by reducing Au and Pt precursors with two reducing agents in a one-pot synthesis. Hydrogen was used for the reduction of Pt (II), whereas acrylate was for the reduction of Au (III). The latter reaction was specified to be catalyzed by the formation of Pt from the reduction of Pt(II). AuPt NPs with bimetallic compositions from ~4 to 90% Au and particle size ranging from 2 to 8 nm have been demonstrated. Generally, for all mentioned alloy synthesis above, the size and composition of the AuPt alloy NPs can be controlled by controlling the synthetic feed ratios and metal precursor concentrations. Although the correlation between the particle size and the composition is not clearly understood (the correlations also change with different process), it might be due to a difference in the nucleation process.

To obtain a core shell structure, seeding growth method is usually adopted. A metal nanoparticle serves as the seed, and the salt of a second metal is chemically reduced on the core surface to form the shell layer. The growth of the shell layer can occur either with the core in a solution or assembled on a substrate. The size of the core-shell particles can further be modulated by controlling the ratio of the amount of the seed and the metal ion. For example, Zhang et. al [49] used 12 nm Au as seeds, and then deposition and reduction of Pt by ascorbic acid to obtain Au core/Pt shell bimetallic structure. Nonetheless, sequential reduction for bimetallic synthesis sometimes obtains structures other than core-shell, including dendritic structure and alloy (as illustrated above). A good example is from Zhou's group [50] who modified this route and used

strong reducing agent to make dendritic structure as well as alloy with different particle sizes of pre-synthesized Au. That is, when the Au seeds used for Pt deposition are small enough, the faster atomic diffusion inside the bimetallic NPs will result in an AuPt alloy formation. Otherwise, AuPt dendritic structure (similar to core/shell structure) is favored since the atomic diffusion is slowed down.

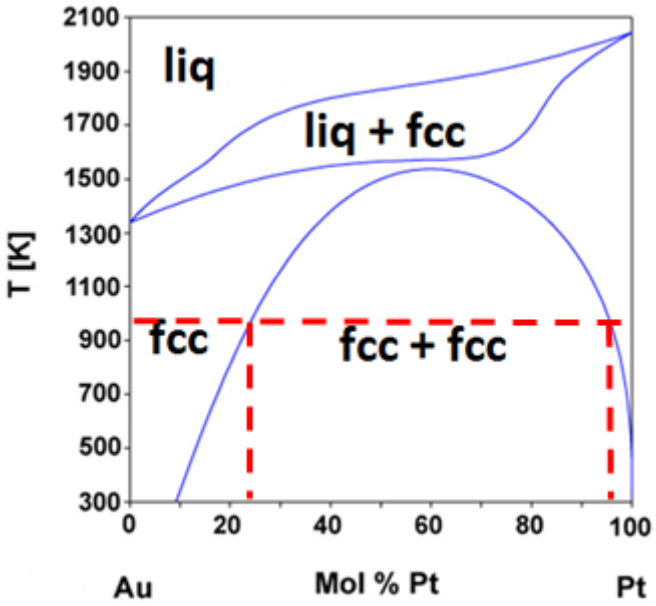


**Figure 5.** Phase diagram of Au and Pt. Red dash line shows the critically stable composition of bimetallic Au and Pt at 700℃ (973K)

### 1.5.3 Bimetallic phase properties

Au-Pt phase diagram exhibits a miscibility gap over a wide range as shown in Figure 5. Therefore, how the phase properties of AuPt bimetallic NPs change with temperature is another key point for bimetallic catalyst applications. Recently, Wanjala et. al used carbon supported bimetallic AuPt to study the evolution of phase segregation as a function of temperature by a series of experiments [51] (Figure 6). It was shown that the bimetallic NPs finally formed a Pt-

rich core and an Au enriched shell rather than separate Au and Pt NPs after an elevated temperature treatment. The experimental result is consistent with molecular dynamic simulation showing that Pt-core/Au-shell structure is the most stable one, whatever the initial structures (such as decahedra, icosahedra, and cuboctahedra) (Figure 7) [52]. Liu et. al concluded that the large difference of melting point of gold and platinum dominating the melting mechanism of the bimetallic NPs. This was again confirmed by Xia et. al who used thermodynamic model and an analytic embedded atom method (AEAM) to estimate the alloying ability and phase stability of AuPt alloy via calculating its heat of formation [53]. They pointed out that the heat of formation for a alloyed AuPt particle depends on not only the composition of the alloy, but also particle size, suggesting that there is a big difference between of immiscible alloy in the bulk and the nanoscale. The alloyed AuPt hence is able to be made over entire composition range if the particle size is less than 6 nm according to their report. Nonetheless, at sufficiently high temperature, nanoscale AuPt tends to form the Pt-core/Au-shell structure which is identical to Liu's simulation and Wanjala's experimental results.

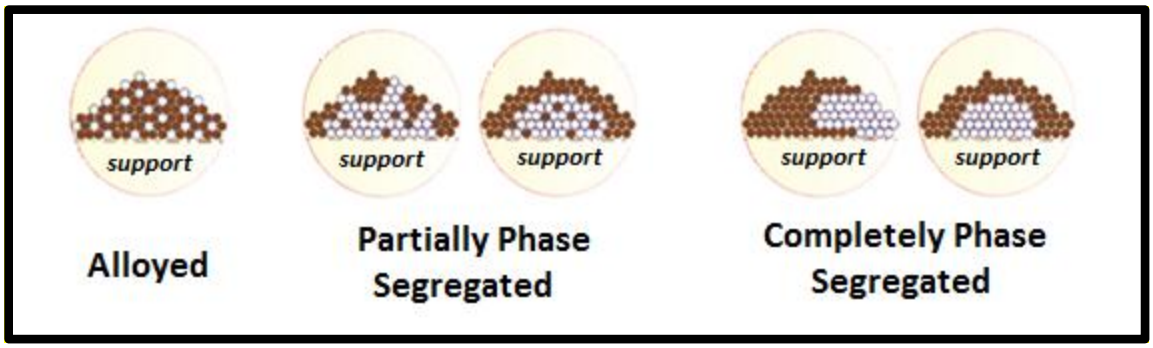


**Figure 6.** Idealized illustrations of the nanoscale alloyed, partially alloyed/partially phase segregated, or completely phase segregated bimetallic metals on a support. Adapted from [51]

Unfortunately, current experimental studies regarding bimetallic AuPt phase behaviors were all operated at different experimental conditions. Hence, the extent of phase segregation of

AuPt NPs varied with experimental conditions and thus different conclusions were made. For example, as-synthesized Au(core)-Pt(shell) NPs with larger size evolve into Au- and Pt-rich crystals separated by a flat interface after calcination above 600℃ under static helium [54]. The alloy AuPt NPs annealed at 700℃ in vacuum for 24 h exhibits phase segregation into an Au-rich alloy and an essentially pure Pt component [47]. The $AuPt/SiO_2$ made by the incipient wetness technique in Schwank's group showed a complete phase segregation and become separate Au and Pt NPs for an Au:Pt=0.3:1, but only some Au segregated out from the bimetallic NPs if Au:Pt=0.7:1 after the reduction under flowing hydrogen at 400℃ [55]. Malis et. al further used the real time x-ray diffraction to study the phase segregation of AuPt NPs on different supports [56]. It is found that various support properties would also result in different extents of phase segregations. For example, alumina supported AuPt NPs exhibit a rich phase behavior and even completely phase segregation after high temperature treatments. Instead, silica supported AuPt NPs synthesized over a wide composition in their report remain alloyed even after annealing at 700 ℃ which is different from Schwank's conclusions. Obviously, these results motivate further research to improve our understanding of bimetallic AuPt phase behavior.

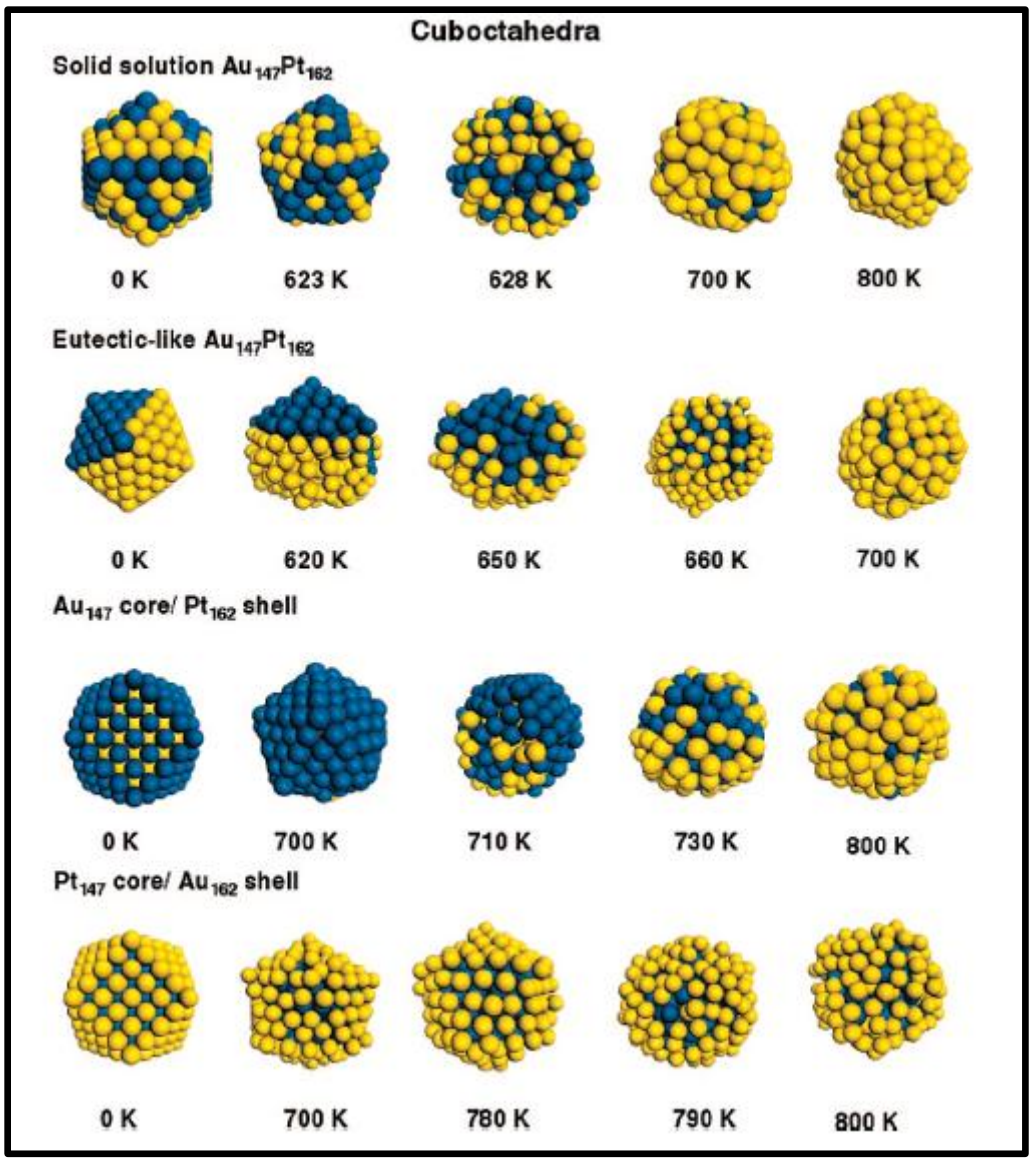


**Figure 7.** Structure transformation of Au-core/Pt-shell, eutectic-like, and solid solution clusters during heating processes [52]

# 2.0 OBJECTIVES

Previous research in our group [41] demonstrated that metal NPs can be stabilized towards high temperature conditions by alloying the particle with a second higher melting metal component. For instance, the low melting Pt is stabilized by the high-melting Rh, and an alloyed RhPt nanoparticle with sufficiently high Rh/Pt ratio shows an excellent stability at temperatures as high as 850℃. This stabilization occurs via "bleeding out" of low-melting Pt resulting in an increase in Rh content in the remaining NPs as the temperature increased. This 'distillation' of Pt from PtRh NPs results in a sacrificial self-stabilization of the bimetallic NPs. In our previous work, this alloying approach was observed to be efficient in these perfectly miscible systems, but no information about immiscible systems was reported. As miscibility between the metals can be expected to impact the alloying/de-alloying behavior, the first objective of this thesis is to evaluate if the alloying approach is also applicable to immiscible systems. Staying with Pt as one metal (in agreement with our previous studies), we selected Au as the second metal based on the fact that alloys show a wide miscibility gap over a large temperature range.

Furthermore, Au catalysts show high activity in WGS at low temperature but deactivates quickly at higher temperature. In contrast, Pt catalysts are much more stable at high temperature, but the high activation energy reduces their activity at low temperature. The second objective of this thesis is thus to target a possible synergistic effect between Au and Pt through alloying to obtain a catalyst with high stability as well as improved low-temperature WGS activity. Again,

the wide miscibility gap of Au and Pt can be expected to impact also the performance of AuPt bimetallic catalysts in WGS.

In the present work, AuPt bimetallic NPs were first synthesized in an aqueous solution and then dispersed on silica and ceria through impregnation. The self-stabilization approach was evaluated by studying this bimetallic system as a function of calcination temperature and duration. Comparison between the bimetallic AuPt on $SiO_2$ and ceria was adopted to identify the impact of the support on the phase behavior of the nanoparticle. Finally, the consequence of bimetallic phase behavior on catalytic activity and stability of $Au_nPt_{100-n}$ over the two supports in WGS was explored in fixed-bed reactor studies.

# 3.0 EXPERIMENTAL

## 3.1 MATERIALS AND SYNTHESIS

### 3.1.1 Materials

Gold chloride trihydrate ($HAuCl_4 \cdot 3H_2O$, >99.9%), Chloroplatinic acid hexahydrate ($H_2PtCl_6 \cdot 6H_2O$, P5775), polyvinylpyrrolidone (PVP, M.W. 55000), cerium nitrate hexahydrate ($CeN_3O_9 \cdot 6H_2O$ , >99.0%) and silicon dioxide (nanopowder) were purchased from Aldrich. sodium hydroxide (pellets, 98%) and sodium borohydride ($NaBH_4$, 98%) were from Alfa-Aesar. All reagents were used as received without further purification.

### 3.1.2 Syntheses

Ceria nanorods were synthesized by a hydrothermal method, as adapted previously in our lab. Briefly, 1.5 g cerium nitrate hexahydrate was dissolved in 8 ml deionized water and 60 ml of NaOH solution (3.5 M) was rapidly added under vigorous stirring. After 30 min of stirring, the slurry was transferred into a 100 ml autoclave, heated to 100℃ under autogenous pressure for 24 h, and then allowed to cool to room temperature. The product was washed by DI water and collected via centrifugation to remove any ionic remnants until the pH of the solution was 7.0. After drying at 80 ℃ overnight and calcination at 400 ℃ for 2 h, the final product was obtained.

The PVP stabilized $Au_nPt_{100-n}$ were prepared in an aqueous solution by reducing Au and Pt precursors with excess sodium borohydride. For example, to prepare 1:1 Au:Pt NPs, firstly, 0.625 ml of a 10 mM $HAuCl_4$ solution and 0.625 ml of a 10 mM $H_2PtCl_6$ solution was added to 10 ml of DI water with stirring. Next, 2.5 ml of a 1.39 mM PVP solution ($6.95\times10^{-7}$ mol) was added. This mixture was then stirred for 30 min at 0℃. 1.25 ml of a fresh 0.10 M sodium borohydride solution ($2.5\times10^{-5}$ mol) was added. After stirring for an additional 30 min, the 1:1 AuPt NPs were obtained. Pure Au and Pure Pt NPs were prepared as stated above keeping the total molar amount of metal salt constant. Besides spreading the bimetallic NPs on supports, some bimetallic samples synthesized in the same way were dried at 70℃ under vacuum overnight for Energy Disperse Analysis of X-rays.

The as-synthesized colloid was then centrifuged in a centricon (Ultracel-10K, Amicon Ultra Inc.) to wash away ionic impurities. The dark brown powder product was re-dispersed in DI water with PVP. The colloid was again centrifuged and re-dispersed three times as described above. The final amount of colloid was dispersed on different supports with specified metal loadings (5 wt% and 1%wt) and then dried in an oven at 100℃ under vacuum overnight.

The protocol for phase studies and activity of AuPt bimetallic NPs involved assembly of as-synthesized NPs on supports, followed by thermal treatments at controlled temperatures and atmospheric pressure. The heat treatment included heating the samples from room temperature to specified temperatures under air (0.1 grade) and holding for a specified time.

## 3.2 CHARACTERIZATION

Temperature-programmed reduction by hydrogen ($H_2$-TPR) was conducted for characterizing the reducibility of as-synthesized ceria. TPR was operated with a Micromeritics Chemisorb 2750 system equipped with a thermal conductivity detector. During the TPR analysis, the samples were first oxidized in 5% $O_2$/He at 450℃ for 2 h, and then TPR was performed by heating the sample (100 mg) at 5 ℃/min to 900 ℃ in a 10% $H_2$/Ar flow (30 ml/min). A cold trap filled with acetone-dry ice mixture was placed between reactor and TCD to remove water vapor.

The actual compositions of Au and Pt in the bimetallic system were determined by Energy Disperse Analysis of X-rays (EDAX) equipped on Philips XL-30 field emission scanning electron microscope (SEM). UV–vis spectra were obtained by using a Beckman Coulter DU 720 general purpose UV/Vis spectrophotometer with a scan range of 200–1000 nm. X-ray diffraction (Philips PW1830) measurement was used to identify crystalline phases in the materials. The diffraction patterns were record in the range of $30\text{-}50^0$ with a step of $0.02^0$ (2θ). All XRD patterns shown in this paper are subtracted from the background in order to obtain a better fitting of curves. The particle size of Au, Pt and bimetallic AuPt NPs were estimated from this data via standard Debye-Scherrer formula.

Transmission electron microscopy was performed on JEOL-2000FX and JEOL JEM-2100F electron microscopes. Samples were dispersed on a copper type-B support grid (Ted Pella Inc.).

CO chemisorption was conducted for catalysts after WGS with a Micromeritics Chemisorb 2750 system equipped with a thermal conductivity detector. The CO TPD experiment includes three consecutive steps: pretreatment, CO chemisorption and CO TPD. The sample was first oxidized in 5% $O_2$/He to clean the surface impurities and then reduced in 10% $H_2$/Ar. The

pretreatment conditions were slightly adjusted for the different support, silica (at 600℃) and ceria (at 500℃). After cooling in He to room temperature, CO pulse chemisorption was then carried out until the sample was saturated. The TPD was finally performed by heating the sample (50mg) with a ramping rate of 40K $min^{-1}$ to 900K and 1300K for silica and ceria supported catalysts under a He flow (50ml/min), respectively. All of the desorbed species were monitored by a quadrupole mass spectrometer (Omnistar, Balzers).

## 3.3 CATALYTIC ACTIVITY MEASUREMENTS

Water gas shift tests were carried out in a 5mm ID quartz glass tube inserted into a high-temperature tube furnace at ambient pressure. The catalyst powder (50 mg) was supported within the tube on either end by quartz glass felt plugs. Water was injected via a syringe pump (Braintree Scientific, Inc.) and vaporized in a heated line before entering the reactor. The composition of the mixture after water addition was 10.78% $H_2O$, 2.08% CO, and 87.14% He. The total flow rate of gas was typically around 100 CCM resulting in space velocities of ~150,000 $h^{-1}$. The exit gas passed through a U-tube filled with silicon beads to eliminate $H_2O$ from the stream and then was analyzed by an Agilent 3000A Micro GC equipped with thermal conductivity detector (TCD). The CO conversion was measured repeatedly until stable within 3% difference. It should be noted that CO conversion over silica supported catalysts (Pt-related) show large fluctuation as high as 15% at temperatures above 550℃ during the water-gas shift reaction. No methane was detected at any conditions used in this work. The inert helium feed is used as an internal standard, and is used to calculate the total gas flow rate after water condensation and to back-calculate the concentration of water leaving the reactor.

# 4.0 RESULTS

## 4.1 SYNTHESIS

### 4.1.1 Bimetallic Au and Pt nanoparticles

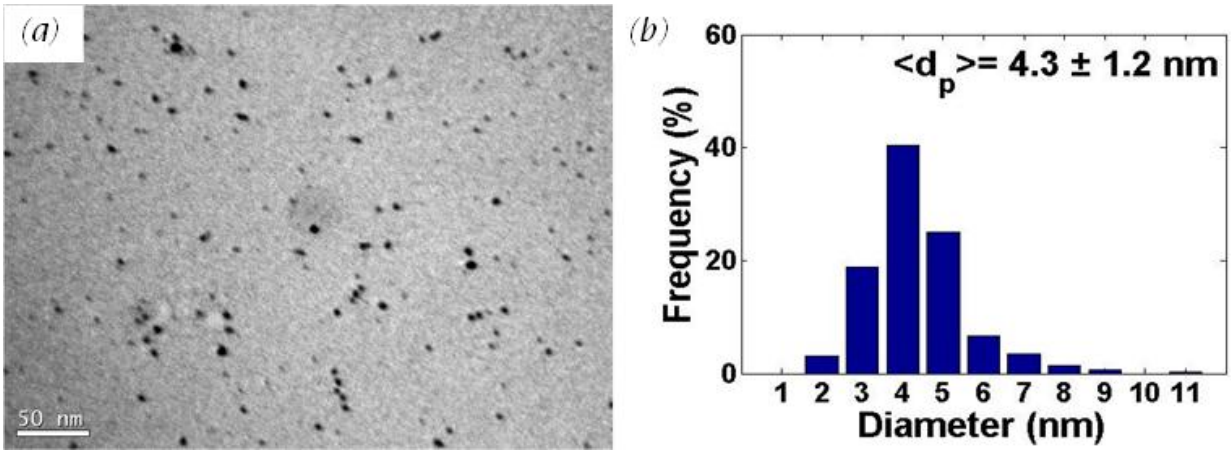


**Figure 8.** (a) TEM for as synthesized AuPt(1:1) bimetallic NPs, and (b) its particle size distribution

AuPt bimetallic NPs were prepared in aqueous solution and reduced by sodium borohydride with PVP as protecting agent. Figure 8a shows the TEM image of bimetallic AuPt NPs and the particle size range of these bimetallic NPs shown in Figure 8b, small (4.3 nm) and uniform NPs were obtained.

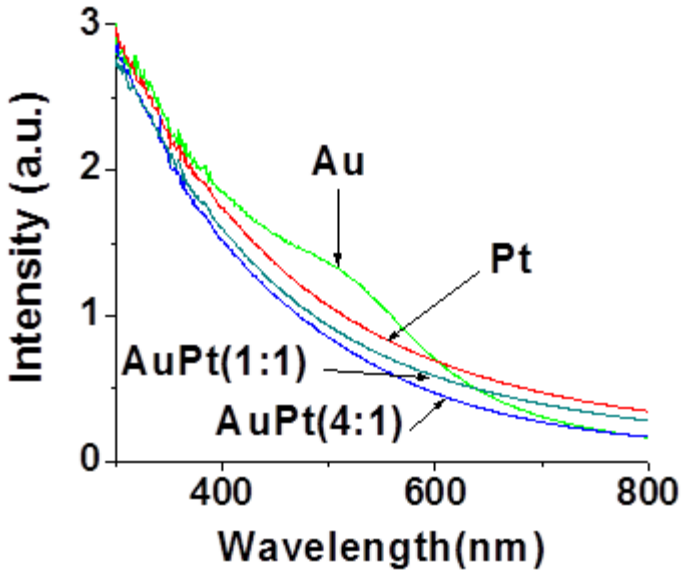


**Figure 9.** UV-vis for as-synthesized NPs

UV-visible spectra of Au NPs, AuPt NPs and Pt NPs synthesized in a similar way are shown in Figure 9. Au NPs have an observable surface plasma resonance band at about 520 nm. The absence of this band in the cases of bimetallic AuPt NPs even with the ratio 4 to1 indicates the change of electronic property of Au surface induced by Pt [50] and hence implies formation of bimetallic NPs.

The compositions of as-synthesized bare $Au_{48}Pt_{52}$ NPs (nominal ratio of Au to Pt is 1:1, AuPt(1:1)), as-synthesized bare $Au_{80}Pt_{20}$ NPs (nominal ratio of Au to Pt is 4:1, AuPt(4:1)), and 5% $Au_{68}Pt_{32}/CeO_2$ (nominal ratio of Au to Pt is 2:1, AuPt(2:1)) calcined at 400℃ were confirmed by EDAX, demonstrating the coexistence of Au and Pt in the product as well as the consistency between the nominal compositions and resultant ones. For all measured samples, the bimetallic composition was controllable by the feed composition used for the AuPt bimetallic synthesis.

### 4.1.2 Nanostructured ceria

Ceria in this thesis were synthesized through a facile hydrothermal approach. The $H_2$-TPR result for our as-synthesized ceria is shown in Figure 10. It should be noted that the peak position of ceria nanorod and nanoparticle were indicated to be around 350℃ and 420℃ from our previous experiments, respectively. However, the peak of our ceria sample spans from 350℃ to 420℃, which indicates a mixture of rods and particles. Their morphologies can be confirmed with TEM image, for example, 5% AuPt(1:1)/$CeO_2$ is shown in Figure 11, and the ceria is actually consisted of both some rod-like NPs and nanorods.

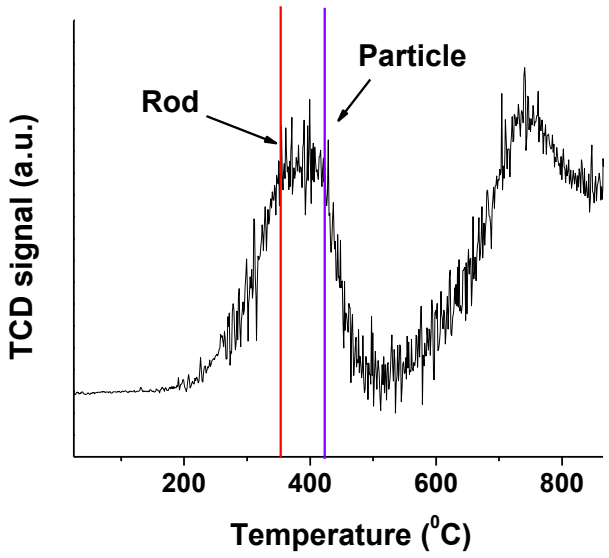


**Figure 10.** $H_2$-TPR profile of as-synthesized ceria

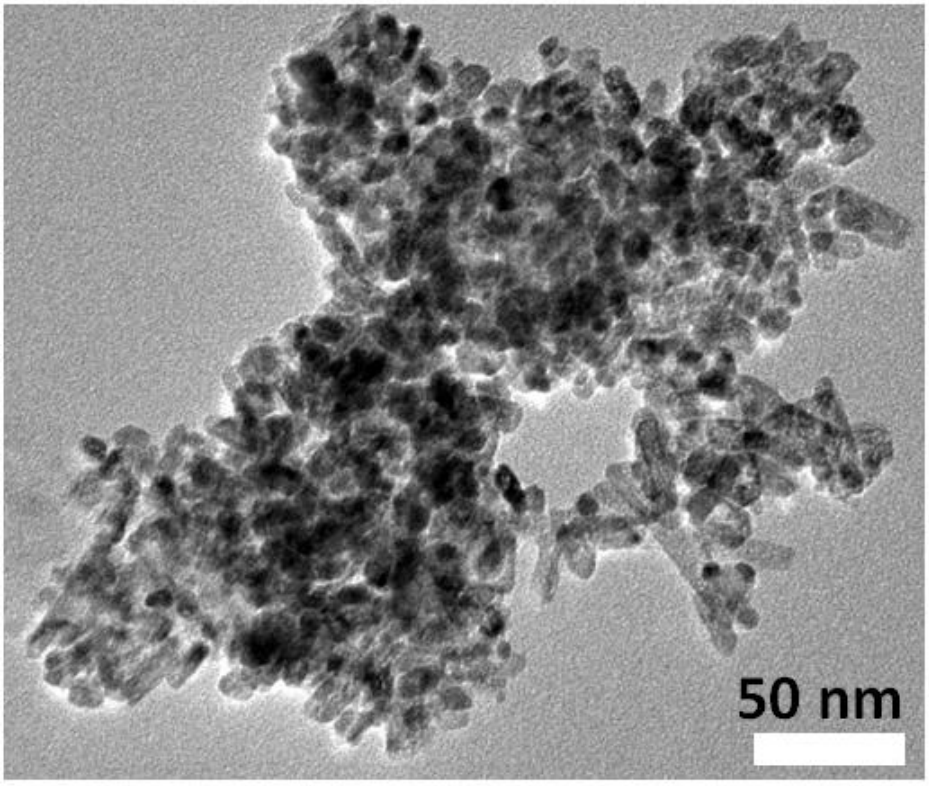


**Figure 11.** TEM image of 5% AuPt(1:1)/$CeO_2$

## 4.2 NANOCRYSTAL PHASE STUDIES

### 4.2.1 Phase stability I: 5% AuPt on $SiO_2$

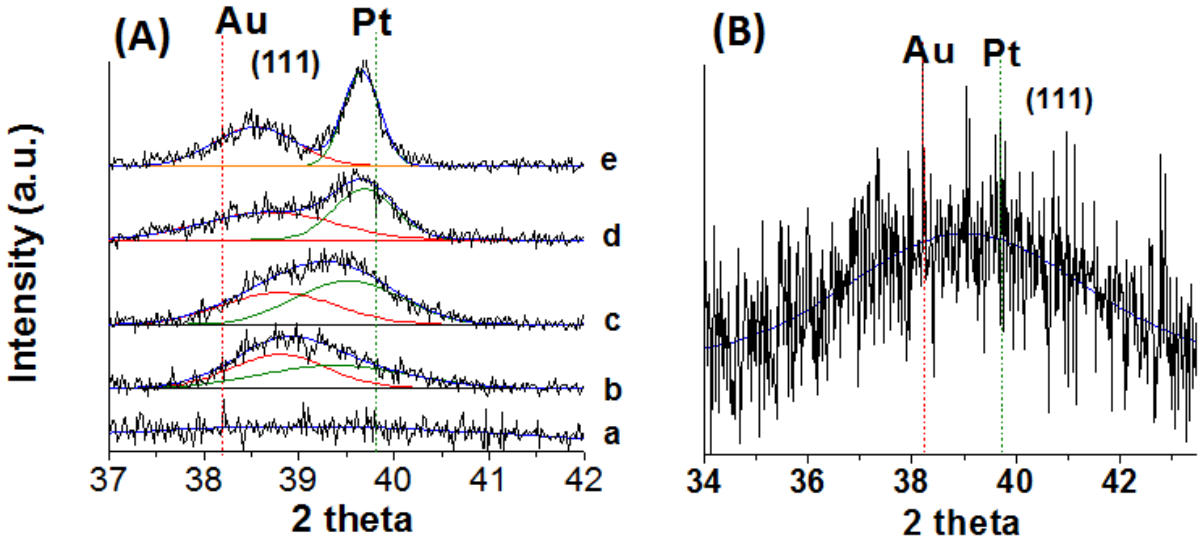


**Figure 12.** (A) XRD for 5% AuPt(1:1)/$SiO_2$, (a) uncalcined, (b) calcined at 400℃ for 4.5hr, (c) 500℃ for 2hr, (d) 500℃ for 24 hr, and (e) 700℃ for 2hr. (B) The enlargement of diffraction curve of uncalcined sample

Amorphous silicon dioxide does not give rise to reflections in XRD [57] and gives a strong contrast against metals under TEM operation. Furthermore, its weak interaction with metals in contrast to that of ceria is important for studying the support properties on bimetallic phase behavior. Therefore, to investigate the bimetallic AuPt NPs, silicon dioxide were first adopted to study the structure of the AuPt bimetallic NPs, as well as their phase evolution as a function of temperature. Figure 12B shows the XRD pattern of the as-synthesized 5% AuPt/$SiO_2$ with a nominal ratio of Au/Pt = 48:52. The maximum (39.02) of the peak is right in between the {111} reflection of Au (2θ = 38.21) and that of Pt (2θ = 39.79), which suggests these 1 to 1 ratio NPs are bimetallic alloy instead of two separate Au and Pt. This XRD curve also reveals that the

resultant Au and Pt particles are face-centered cubic although the broad peak indicates they are in small size [44].

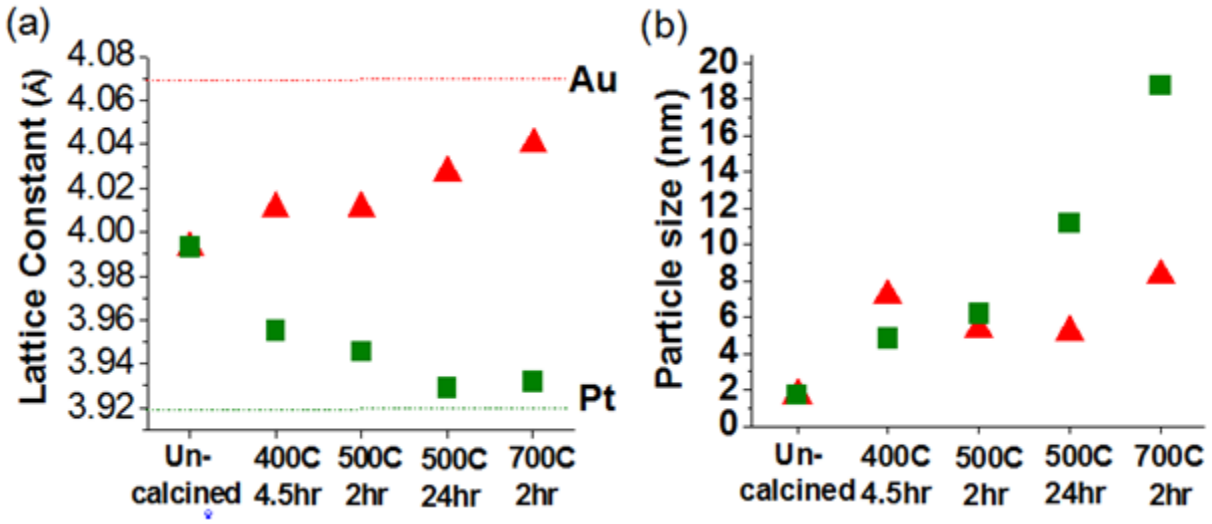


**Figure 13.** (a) Lattice constant (b) and estimated particle size of 5% AuPt(1:1)/$SiO_2$ from XRD data. Red triangle representing the Au-rich phase and green square representing the Pt-rich phase are extracted from the XRD pattern in Figure 12A

In order to understand the nanoscale phase evolution of silica supported bimetallic AuPt(1:1) synthesized in our method, the catalyst was treated at different temperatures under air and characterized by XRD analysis. It should be noted that all samples before calcination for studying the phase properties were still protected by PVP, which was burned away during heat treatments. The XRD patterns shown in Figure 12A were fitted with Gauss function to acquire the detailed phase changes of bimetallic AuPt NPs. The result reveals that 5% alloyed AuPt(1:1) NPs on silicon dioxide was not stable even at the temperature as low as 400℃, which contradicts the result observed by Malis et. al whose bimetallic NPs on silica are very stable up to 700℃ [56]. It is possible that adopting different synthesis approaches to produce AuPt bimetallic NPs or the heat treatments under different environments (heat treatment at 300℃ for an hour under 20% $O_2$, followed by a high-temperature treatment at 400℃ -700℃ under He for 30 mins in

Malis' work) may cause a delayed phase change, though the tendency of phase behavior should be similar.

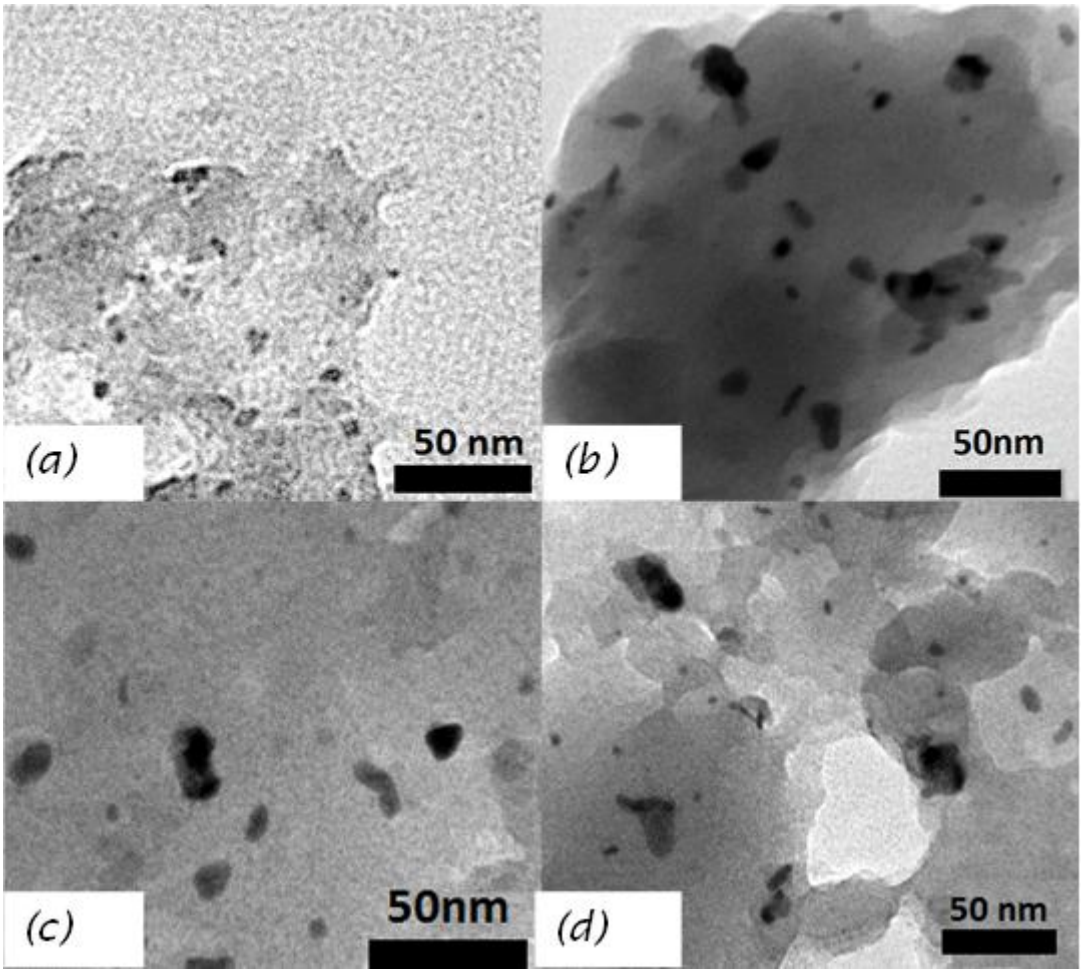


**Figure 14.** TEM images for 5% AuPt(1:1)/$SiO_2$ calcined at 400℃ for 4.5hr (a), at 500℃ for 2hr (b), at 500℃ for 24hr (c), at 700℃ for 2 hr (d)

The shift of the two splitting peaks is quantified by the corresponding lattice constant (see Figure 13a). One can clearly see that during the thermal treatment, the original bimetallic NPs become two different groups of NPs with an Au-rich population and a Pt-rich one. Either a higher temperature or an extended calcination time in our studies not only resulted in a higher degree of particle sintering (see Figure 13b and Figure 14) but also in more severe phase segregation. In other words, with increasing time or temperature for heat treatment (e.g. 2h at

500℃ vs. 24h at 500℃), the two phases go toward the compositions consistent with the thermodynamic properties described in phase diagram of Au and Pt. Figure 5 shows the stable phase composition at the highest temperature applied here, 700℃. The stable compositions at this temperature are 23% Pt (77% Au) and 96% Pt (4% Au), which are close to the composition in our AuPt/$SiO_2$ system treated at 700℃, 20% Pt (80% Au) and 94% Pt (6% Au), respectively.

.

### 4.2.2 Phase stability II: 5% AuPt on $CeO_2$

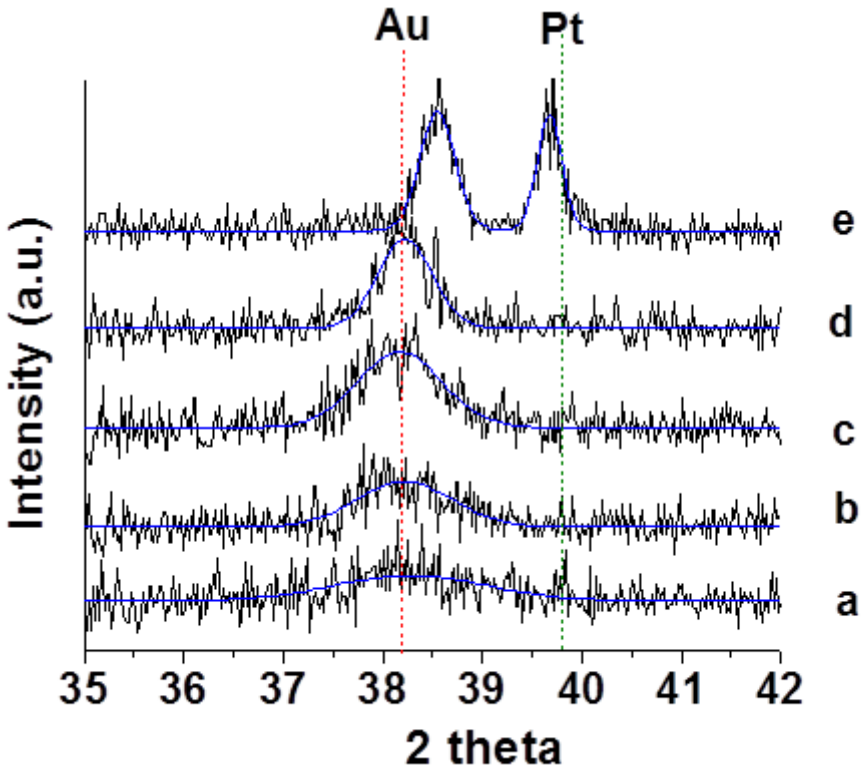


**Figure 15.** XRD for 5% AuPt(1:1)/ $CeO_2$ calined at (a) 400℃ for 2 hr, (b) 500℃, 2 hr, (c) 500℃, 24 hr, (d) 700℃, 2 hr and (e) 900℃, 2 hr

Figure 15 shows a representative set of XRD patterns for 5% AuPt(1:1)/$CeO_2$ with different thermal treatment conditions. Remarkably, only characteristic peak of pure Au can be observed for calcination temperatures below 700℃. The lack of Pt reflections suggests that Pt forms very small clusters below the detection limitation of the XRD instrument (≤ 2 nm). To compare the support effects on the bimetallic phase behavior at the transition temperatures (i.e. 400℃ -700℃), the lattice constant and particle size calculated from XRD patterns are shown in Figure 16. Firstly in Figure 16b, the average particle sizes of Au grows apparently with thermal treatments while the Pt on ceria remains very stable up to the temperature as high as 700℃ indicated by the absence of any Pt reflection in this temperature range. In Figure 16a, the lattice

constant of Pt-rich bimetallic phase appears only at 900℃, which means phase separation of ceria supported AuPt(1:1) begins below or at 400℃, with some Au phase-separating from original alloyed AuPt.

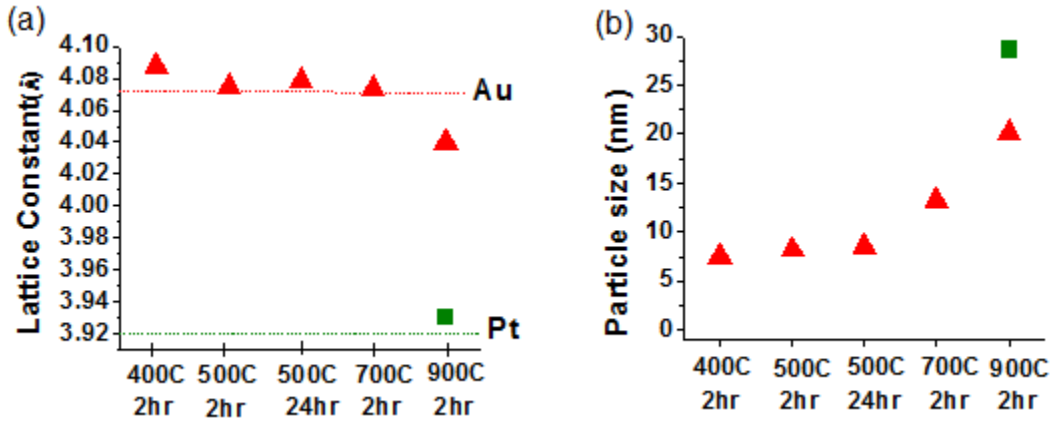


**Figure 16.** (a) Lattice constant and (b) estimated particle size of 5% AuPt(1:1)/$CeO_2$ by Scherrer formula from XRD data. Red triangle representing the Au-rich phase and green square representing the Pt-rich phase are extracted from the XRD pattern in Figure 15

To further analyze the details of the phase structure of ceria supported bimetallic AuPt NPs at the transition temperature, Figure 17A shows the TEM images for 5% AuPt(1:1)/$CeO_2$ calcined at 400℃ (to facilitate distinction of bimetallic NPs from ceria, an area with well-formed nanorods is shown here). Particles with larger size (5-8 nm) and some very small ones are visible (< 2 nm). In particularly, the size of larger NPs is quite close to the size estimated from XRD for Au phase in Figure 16b. The compositions of these NPs can be confirmed by the d-spacing of corresponding particle size, which is illustrated in the inset of Figure 17B. The d-spacing of pure gold and pure platinum are reported to be 0.235nm and 0.226nm, respectively, where the one of Au is consistent with the representative example shown here. This suggests that AuPt(1:1) after thermal treatments may undergo a complete phase separation and the separated Au phase as shown in XRD is from the bleeding out Au NPs . However, the ultra-small particles are too small

to be analyzed, and hence it is impossible to identify their chemical composition accurately. Nonetheless, from the above observations, it is clear that ceria supported bimetallic AuPt NPs behave differently from the partial phase segregation of bimetallic AuPt dispersed on silica.

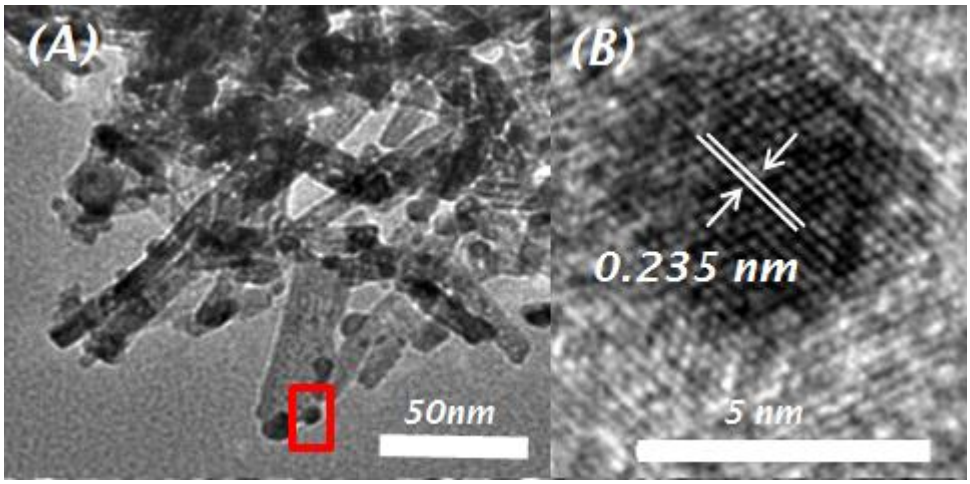


**Figure 17.** TEM images for 5% AuPt(1:1)/$CeO_2$ calcined at (A) 400℃ for 2hr. (B) The enlargement of (A) for {111} plane d-spacing of a 5.6 nm particles

Once the temperature is high enough, Au fuses with those ultra-small NPs again and forms two bimetallic compositions, which is indicated in XRD pattern (e) in Figure 15. In fact, it has been shown that alloy formation in the case of bulk Au and Pt has been observed only at temperatures above 1100℃ (1373K), where Au and Pt are close to miscible zone (see Figure 5) [58, 59]. However, it works for nanoscale Au and Pt at even lower temperature here and the compositions are consistent with those at its corresponding temperature in bulk AuPt phase diagram. This re-alloying also demonstrates that the "missing" Pt in the XRD pattern does exist at lower temperature (i.e. 400℃ -700℃), as also confirmed via EDAX.

## 4.3 CATALYTIC ACTIVITY AND STABILITY TESTS IN WGS

The second objective of this thesis is to use Pt to stabilize Au in high temperature WGS and also improve the reactivity of Pt in low temperature WGS. However, in section 4.2, we found that bimetallic NPs on above two supports undergo different pathways at the transition temperatures but both cases all suffered phase segregation. Bimetallic AuPt on silicon dioxide separated into an Au-rich phase and a Pt-rich phase after thermal treatments, while Au NPs bleeds out as the bimetallic NPs supported on ceria. Thus, we would expect to see a difference between AuPt/$SiO_2$ and physical mixture of Au/$SiO_2$ and Pt/$SiO_2$ on both reactivity and stability in WGS. On the other hand, the bleeding out Au on ceria should make the ceria supported bimetallic catalyst deactivate and the reactivity should be contributed from Au and Pt-rich, respectively. To confirm how the observed phase segregation affects the performance of these bimetallic NPs in WGS, bimetallic AuPt catalysts on the two supports were evaluated in a fixed-bed reactor. In addition, in agreement with typical technical catalyst loading, 1 wt% instead of 5 wt% metal loading is adopted for all catalytic tests.

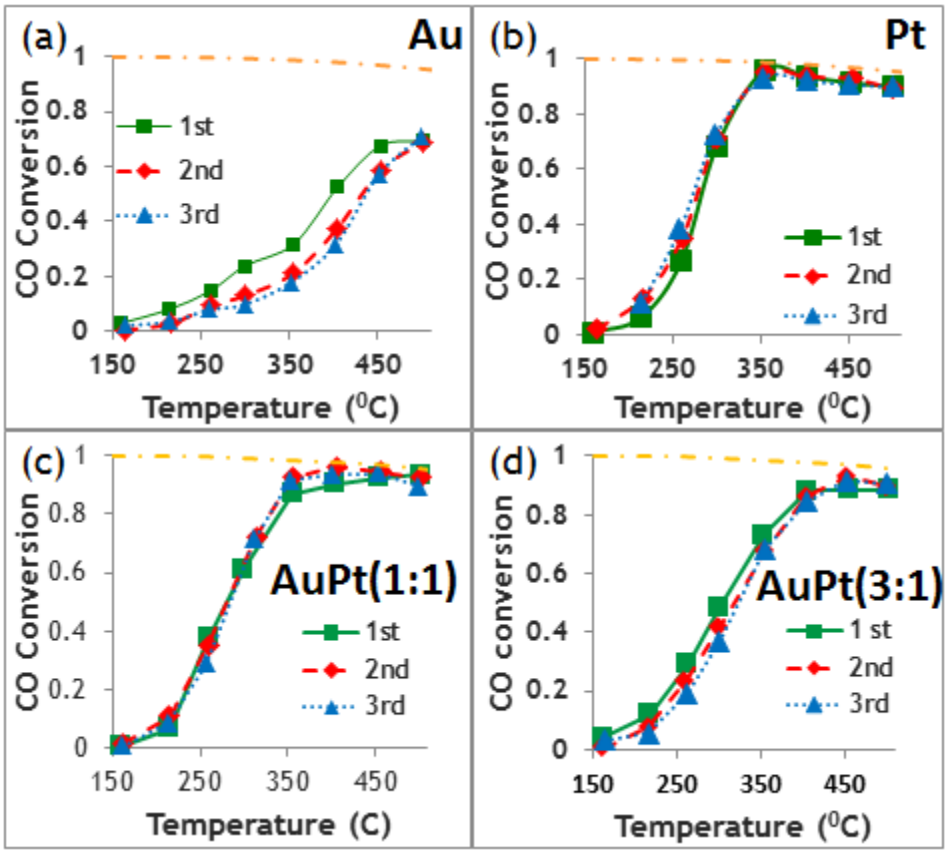


**Figure 18.** Stability for WGS reaction over ceria supported (a) 1% Au, (b) 1% Pt, (c) 1% AuPt(1:1), and(d) 1% AuPt(3:1). The dash-point line in each figure is equilibrium line

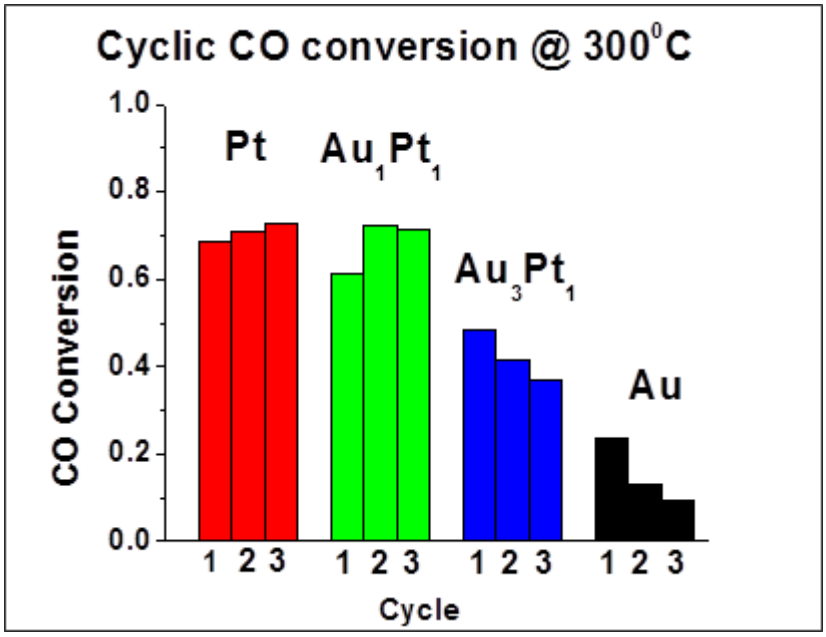


**Figure 19.** CO conversion at 300℃ extracted from each catalytic activity test of ceria supported catalysts

### 4.3.1 $CeO_2$ supported catalysts

Using ceria as the support, the WGS performance and stability of the two separately supported metals, gold and platinum, were first tested and shown in Figure 18. As expected, pure Au catalyst (Figure 18a) deactivates, due to sintering caused by the high mobility of Au at high temperature. In contrast, pure Pt catalyst behaves very stable over three ignition cycles and is even slightly activated at temperatures between 200℃ to 350℃ during WGS cycle as indicated in Figure 18b. To clearly distinguish the changing stability with bimetallic compositions, the representative CO conversion at 300℃ shown in Figure 19 is extracted from each catalytic activity test. Obviously, bimetallic AuPt/$CeO_2$ deactivates but not as fast as the pure Au/$CeO_2$ does. Specifically, AuPt(1:1)/$CeO_2$ in Figure 19 is activated like Pt/$CeO_2$ and then start to deactivate instead of deactivating all the way, suggesting combination of slightly activated Pt and gradually deactivating Au which separates out from the alloyed AuPt. Not surprisingly, the higher the Au content (AuPt(3:1) in Figure 19), the less stable the catalyst would be due to the increasing "bleeding out" of Au NPs. The remaining Pt-rich NPs are then responsible for the relatively high stability of bimetallic catalysts compared to that of Au/$CeO_2$. This stability of AuPt bimetallic catalysts in WGS also agrees well with the above XRD analysis.

The overall performance of these catalysts in WGS is compared in Figure 20. The WGS reaction activities over ceria supported catalysts are ranked to be: 1% Pt ≈ 1% AuPt (1:1) > 1% AuPt (3:1) ≈ 0.5% Pt > 1% Au. The activity of gold was not as good as expected especially at low temperature. This is most likely due to the synthesis method (impregnation) adopted in this study, where larger Au particles were obtained. Nonetheless, the Au catalyst would still agglomerate and deactivate to be similar to that shown in Figure 18a after cycles of WGS, even if the beginning particle were synthesized in a smaller size. That is why the second objective of

this present work was set, to stabilize Au via alloying with Pt. In contrast, the 1% $Pt/CeO_2$ is shown to be not only the most stable one as discussed above but also the most active one over the whole temperature range.

To understand the bimetallic synergistic effect of Au and Pt in reactivity for WGS, 0.5% Pt was also tested. Comparing 0.5% Pt with 1% AuPt(1:1), it was found that the activity of 0.5%Pt was enhanced to be close to that of 1%Pt catalyst by addition of Au. Moreover, the catalytic activity of bimetallic catalysts increases with increasing content of Pt by comparing AuPt(1:1) with AuPt(3:1), which suggests the AuPt bimetallic catalyst is a potential one to replace with the more expensive pure Pt catalysts as sufficiently high ratio of Pt is included.

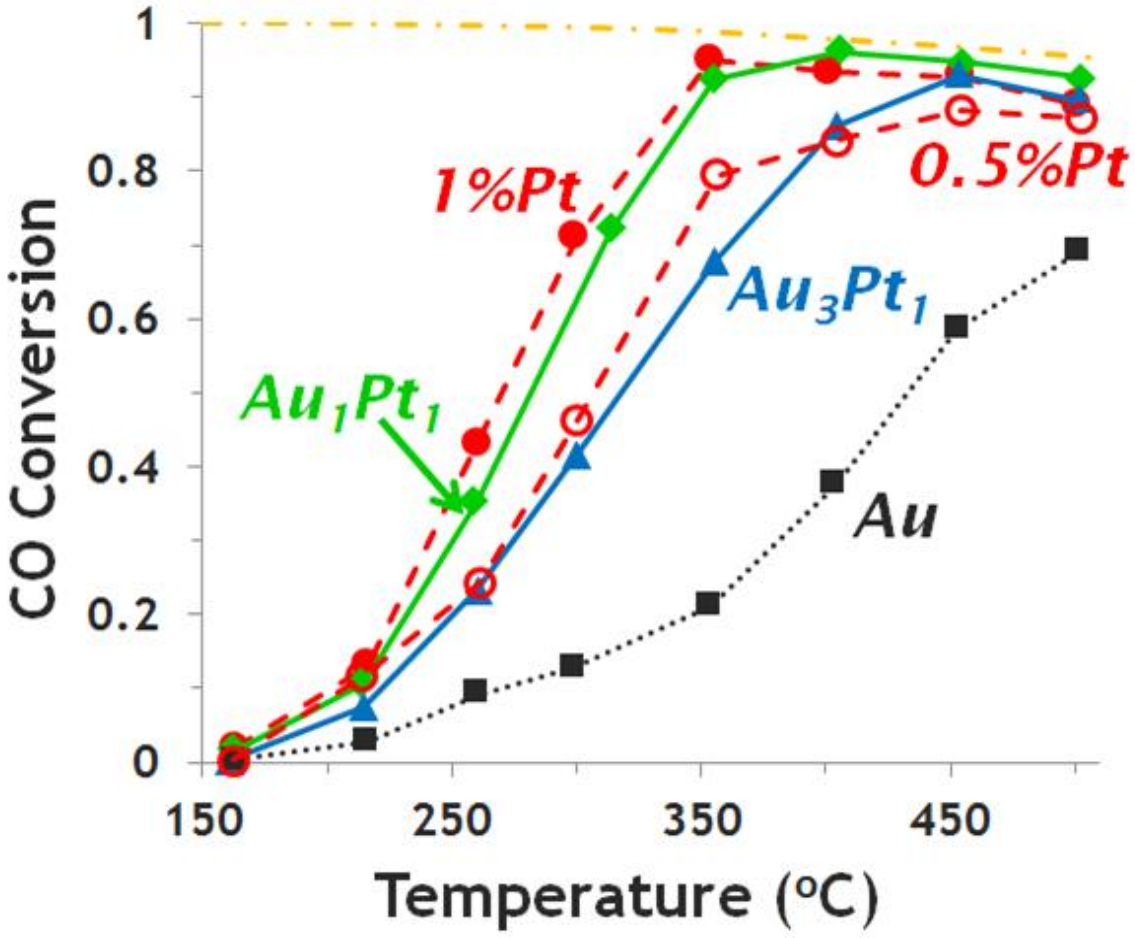


**Figure 20.** Overall comparison of ceria supported catalyst for WGS. Solid-red circle is 1% Pt, open-red circle is 0.5% Pt, solid-square is 1% Au, green-diamond is 1% AuPt(1:1), blue-triangle is 1% AuPt(3:1), and the dash-point line is equilibrium line

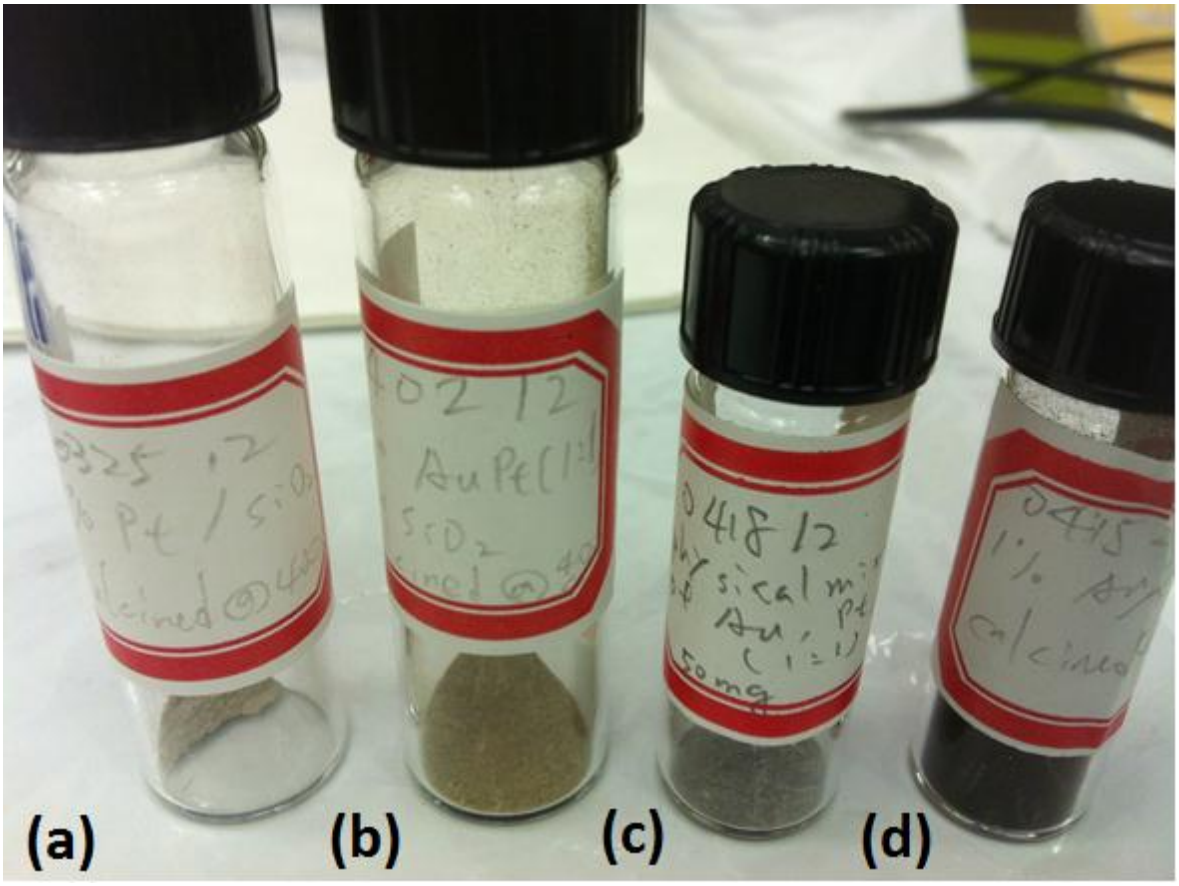


**Figure 21.** (a) 1% Pt, (b) 1% AuPt (1:1), (c) 1% physical mixture of Au and Pt, and (d) 1% Au dispersed on silicon dioxide

### 4.3.2 $SiO_2$ supported catalysts

The silicon dioxide supporting AuPt-related catalysts are expected to show low reactivity for water-gas shift compared to ceria as the support, but they were tested as a comparison since the bimetallic AuPt on silicon dioxide shows an apparently different phase behavior under similar heat treatments. To give a comparable comparison of catalytic activity to 50mg 1% AuPt (1:1)/$SiO_2$, the physical mixture catalyst is made by mixing 25mg of 1% Au/$SiO_2$ and 25mg of 1% Pt/$SiO_2$. All synthesized $SiO_2$ supported bimetallic AuPt catalysts prior to the water-gas shift are shown in Figure 21. One can clearly identify the color of bimetallic AuPt catalyst to be dark

yellow, which is different from the light grey of the physical mixture. This difference in color is one of the evidence that after the pre-heat treatment at 400℃, the AuPt NPs on silicon dioxide still remain bimetallic. Figure 22 shows the WGS performance over each silicon dioxide supported catalyst. It should be noted that CO conversion over Pt-related catalysts show large fluctuation as high as 15% at temperatures above 550℃ during the water-gas shift reaction, the CO conversion reported here was taken by an average of conversions over a during of 2 hr at each temperature. In Figure 22a, 1% $Au/SiO_2$ shows no reactivity even at temperature as high as 600℃. In contrast, the 1 %$Pt/SiO_2$ lights off at around 400℃ (Figure 22b). The activity of these two catalysts is consistent with the result reported by Stephanopoulos' group [28]. Furthermore, the $Pt/SiO_2$ catalyst shows a very stable reactivity over the cyclic reactions, but it is again activated during the $1^{st}$ run reaction. This hence suggests that the re-structuring of Pt NPs is possibly responsible for this changing activity since it occurs on both supports. The physical mixture of silicon dioxide supported Au and Pt (Figure 22d) behaves similar to 1% $Pt/SiO_2$ but with lower activity in WGS. Although half of the physical mixture is the inactive $Au/SiO_2$, 0.5% $Pt/SiO_2$ is apparently enough to show decent activity. Compared to the physical mixture, 1% $AuPt(1:1)/SiO_2$ gives a much lower activity in the WGS in Figure 22c.

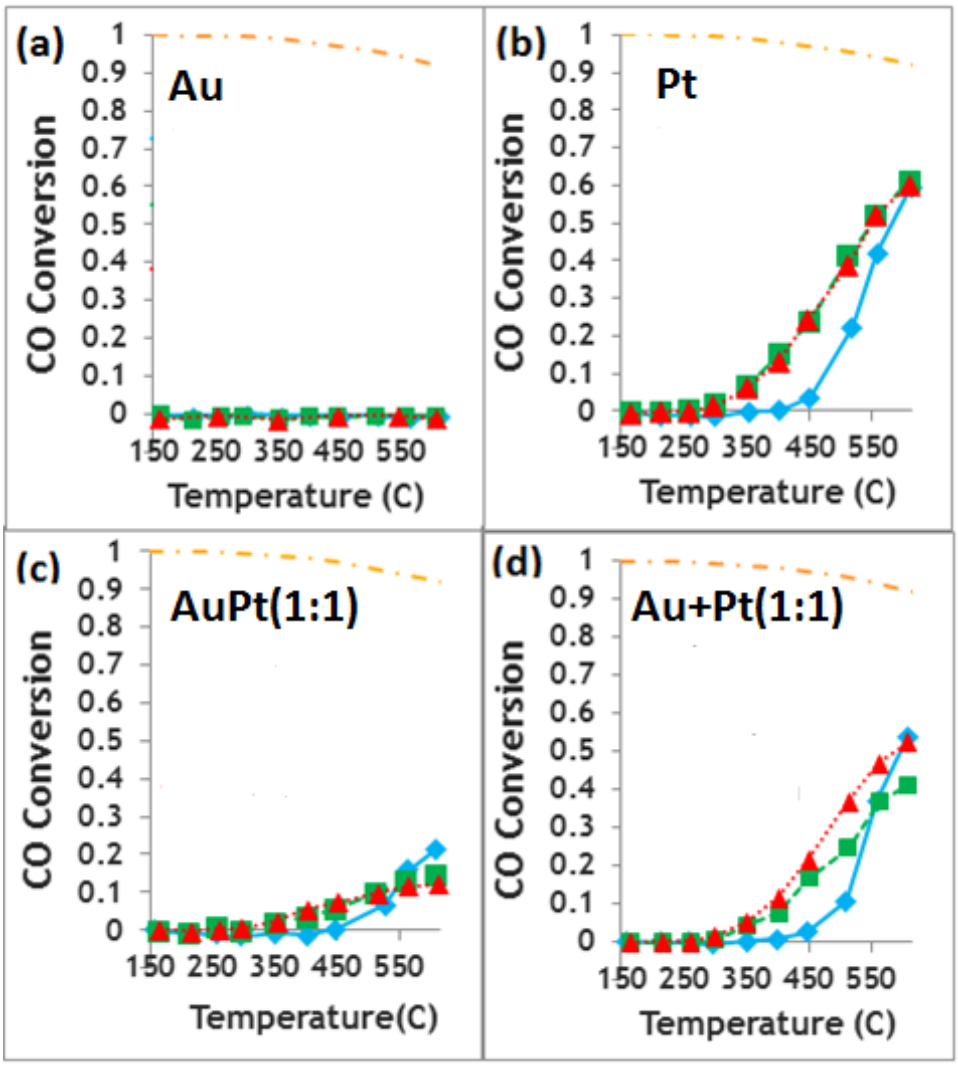


**Figure 22.** Stability for WGS reaction over silica supported (a) 1% Au, and (b) 1% Pt, (c) 1% AuPt(1:1) (d) 1% physical mixture of Au & Pt. Blue-diamond line is 1st cycle, green-square line is 2nd cycle, red-triangle line is 3rd cycle, and the dash-point line in each figure is equilibrium line

These effects can be shown more clearly in the overall comparison of silicon dioxide supported catalysts in Figure 23. The different activity between the 1% AuPt(1:1)/$SiO_2$ and the physical mixture implies that the active site of Pt in the bimetallic catalyst is blocked by Au, which results in a lower activity in WGS. Combining with the previous XRD analysis, it shows not only a strong evidence that the bimetallic phase structure is Pt-rich alloy core and Au-rich shell prior to WGS (i.e. after pretreatment), but also the deactivation of AuPt(1:1)/$SiO_2$ is due to

a further phase separation of AuPt bimetallic NPs to reach thermodynamically stable phases after cyclic high-temperature reaction. It also suggests the bimetallic AuPt on $SiO_2$ behaves similarly to H.B. Liu's theoretical prediction that Pt-core/Au-shell is the most stable state after thermal heating [52].

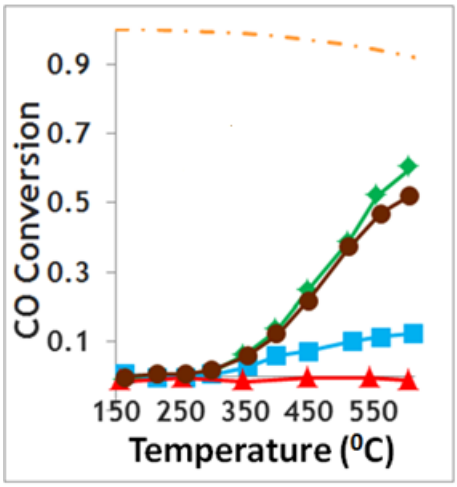


**Figure 23.** Overall comparison of silicon dioxide supported catalyst for WGS. Green-diamond is 1%Pt, red -triangle is 1%Au, blue-square is 1%AuPt, brown-circle is the physical mixture of Au and Pt(1:1), and the dash-point line is equilibrium line

## 4.4 TPD OF CO

To further support the above observation and directly probe the surface composition of the NPs after WGS reactions, CO adsorption/desorption was used as a chemical surface probe. The temperature-programmed desorption (TPD) spectrum of CO is widely used as a sensitive probe of CO–metal interactions in catalysts.

### 4.4.1 $SiO_2$ supported catalysts

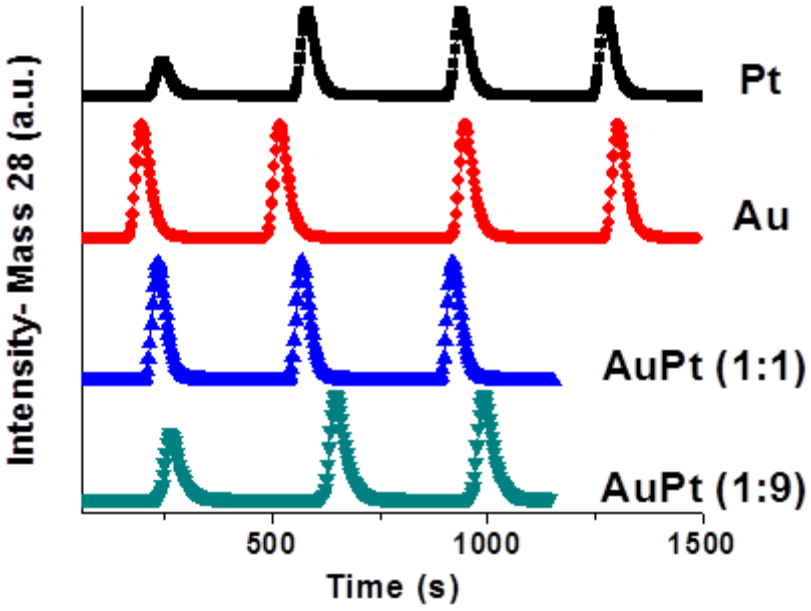


**Figure 24.** CO pulse chemisorption at room temperature for 1% silica supported catalysts until saturated

**Table 1.** Amount of CO adsorption for 1% supported catalysts

| $SiO_2$-based catalysts | Pt | Au | AuPt(1:1) | AuPt(1:9) |
|---|---|---|---|---|
| Volume adsorbed (mL/g STP) | 0.11 | 0 | 0 | 0.0797 |
| $CeO_2$-base catalysts | Pt | Au | AuPt(1:1) | $CeO_2$ |
| Volume adsorbed (mL/g STP) | 0.315 | 0.125 | 0.161 | 0.122 |

As shown in Figure 24 and Table 1, Au catalyst after WGS does not adsorb any CO at room temperature, in agreement with reports on CO chemisorption for $TiO_2$ supported Au at this temperature [60]. In contrast, Pt catalyst does adsorb an observable CO amount. In order to probe the surface composition of bimetallic AuPt NPs after WGS, it is compared with the above two pure metal catalysts. Firstly, no CO adsorbed on the bimetallic AuPt(1:1) catalyst implies the surface composition of this bimetallic nanoparticle is mainly consisted of Au. Moreover, the

lower amount of CO adsorbed on the bimetallic AuPt(1:9) NPs than the 90% of CO adsorbed on Pt NPs (Table 1) manifests another evidence of evolution of phase behavior on bimetallic AuPt NPs. Combining the result of XRD and its performance in WGS with the CO pulse chemisorption analysis, the phase structure of silica supported bimetallic NPs after being in high temperature environment can be further confirmed to be Pt-rich core/ Au-rich shell.

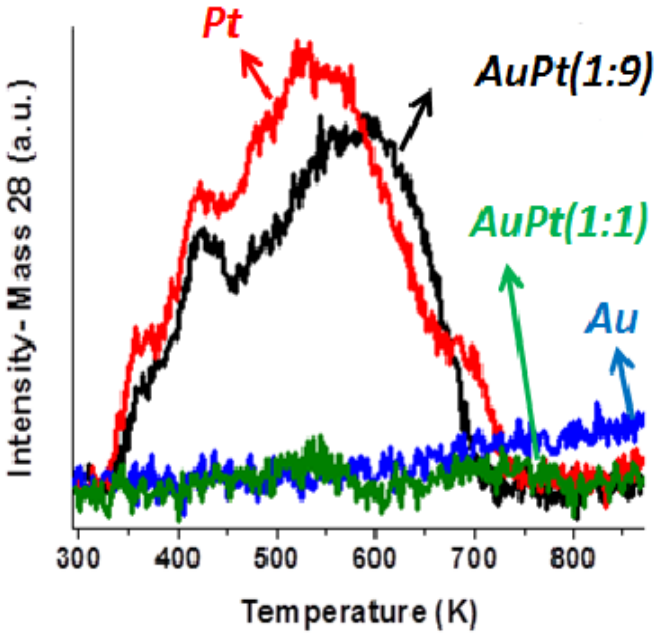


**Figure 25.** CO TPD of 1% silica supported catalysts

From the result of CO chemisorption, as expected, $SiO_2$ supported Au and bimetallic AuPt(1:1) did not release any CO during the TPD experiment in Figure 25. However, if the ratio of gold to platinum is changed to a much lower one, 1:9, CO is adsorbed and the TPD curve is partially shifted in comparison with $Pt/SiO_2$, whose CO TPD curve is close to Pt on alumina [61], with a wide peak between 300K and 800K (i.e. Pt on silica and alumina were shown to have same CO-TPD curve if the same experimental conditions are used [62]). The wide peak in the CO-TPD spectrum of $Pt/SiO_2$ and $AuPt(1:9)/SiO_2$ indicates the activation energy for desorption varies as a function of surface coverage of CO on Pt surface and depends on the size

distribution of the Pt particles [63]. Hence, the phase structure of bimetallic AuPt(1:9) can be presumably assumed to be different from that of AuPt(1:1).

It has been shown that various compositions of bimetallic AuPt NPs may cause different extent of phase segregation, for example, $Au_{25}Pt_{75}$ and $Au_{75}Pt_{25}$ become Pt-core/AuPt-shell and AuPt-core/Au-shell after heat treatments, respectively [64]. This can be further demonstrated with the CO TPD experiment here (Figure 25): due to the low amount of gold in the catalyst, the CO adsorption sites of Pt of AuPt(1:9) could not be completely blocked but only the strong bonding ones, as indicated by the disappearance of step sites on Pt which give rise to the shoulder at ~700K. The shift in the main peak at T~600K suggests that other Pt sites are either partially blocked or electronically modified by Au. Furthermore, the shortage of Au in AuPt(1:9) leaves the terrace sites of Pt open which is reflected in the unchanged TPD peaks at low temperature (350K~400K). Accordingly, the possible phase structure of bimetallic AuPt(1:9) and AuPt(1:1) NPs after WGS is shown in Figure 26.

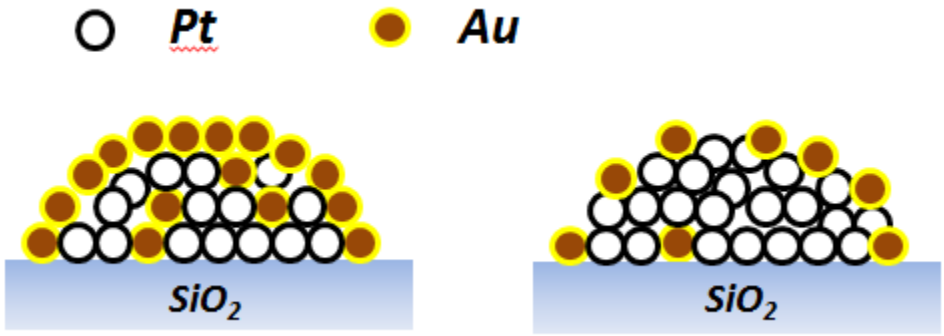


**Figure 26.** Model of silica supported bimetallic NPs after WGS. Left is AuPt(1:1) and right is AuPt(1:9)

### 4.4.2 $CeO_2$ supported catalysts

The ceria supported case is more complicated than the silica supported one. As discussed in the phase study and catalytic activity test sections, some gold phase is completely separated out and the remaining particles are Pt-rich and with very small size. CO pulse chemisorption and TPD was then applied to probe the surface composition of these small Pt-rich NPs after WGS.

First, compare CO chemisorption of Au/ceria and pure ceria in Figure 27 and Table 1, the identical adsorption amount says Au NPs adsorb no CO at room temperature due to weak bonding with CO, which is similar to Au dispersed on $SiO_2$. In contrast, Pt NPs apparently adsorbs a great amount of CO. Assuming the bimetallic NPs had completely separated into physical mixture of Au and Pt after WGS and the separated Pt size is similar to that of ceria supported monometallic Pt, we would expect to see the average adsorption amount (i.e. average=0.220 mL/g STP) of Au and Pt (the identical particle size assumption is reasonable, since we didn't see agglomerated Pt NPs after any thermal treatments below 700℃, suggested by XRD). However, besides the confirmed "bleeding out" Au which contributes nothing to the adsorption amount of AuPt(1:1)/$CeO_2$ in Table 1, the much lower adsorption amount (0.161 vs.

0.220) suggests the remaining Pt-related particles are bimetallic and with Au enriched on the surface.

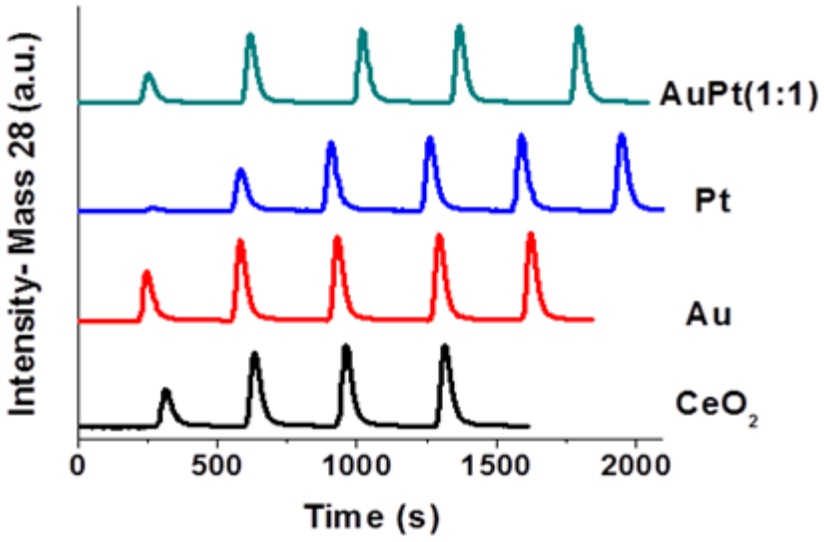


**Figure 27.** CO pulse chemisorption at room temperature for 1% ceria supported catalysts until saturated

TPD following the pulse chemisorption of each catalyst is shown in Figure 28. The CO-TPD spectrum of ceria is featured with three main peaks at 360K with a shoulder at 400K, 590K, and 1023K. In particularly, the maximum at ~1023K also with the release of $CO_2$ indicates the existence of very strongly bound carbonate species on the surface. Both theoretical simulation and experimental measurement for CO adsorption on ceria reveal that only weak adsorption is present on the {111} plane, while weak and strong adsorptions co-exist on the {110} plane and only strong adsorption occurs on the {100} plane [65-67]. Hence, these peaks observed over a wide temperature range here can be attributed to be contributed by both ceria with nanorod ({110}+{100}) and nanoparticle ({111}) shapes as discussed above.

CO-TPD spectrum of Au/ceria was shown to be very similar to ceria itself but with slightly decreased intensity, i.e., the presence of Au does not affect both the adsorption and desorption properties of ceria for CO. On the other hand, the CO desorption properties of Pt

dispersed on $CeO_2$ was previously identified by Zafiris and Gorte [68]. In their report, the 400K feature having been assigned to desorption from Pt atoms with a high coordination number (such as Pt(111)), and the 500K feature assigned to Pt atoms with a low coordination number (such as Pt(110)). However, no desorption properties of Pt can be observed from our $Pt/CeO_2$. Furthermore, in addition to the lower CO and $CO_2$ desorption at ~1023K from the decomposition of strongly bonded carbonate species on ceria, the desorption peak of ceria at ~360K (with a shoulder at 400K) is strongly reduced and that at ~590K is totally suppressed with the decoration of Pt. This is consistent with prior report that $Ce^{+3}$ centers are strongly attenuated while $Ce^{+4}$ sites become completely unavailable for CO adsorption after Pt deposition on $CeO_2$(111) [69].

The TPD curve for bimetallic AuPt(1:1) shows again no desorption spectrum from Pt and is generally similar to that of Pt. However, CO desorption from $Ce^{+4}$ sites (~590K) reappears. In agreement with the conclusion from CO pulse chemisorption above, the decrease of the coverage of Pt on $Ce^{+4}$ sites can be attributed to lower amount of Pt in AuPt(1:1) (i.e. compared to pure Pt) as well as Pt-rich particles decorated with Au on the surface.

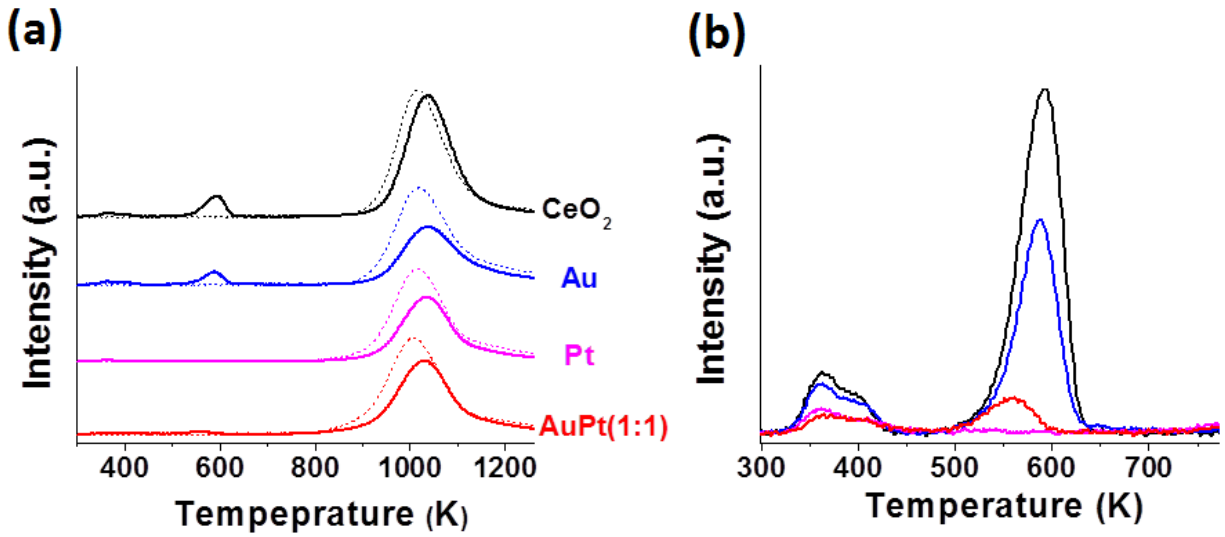


**Figure 28.** CO TPD of 1% ceria supported catalysts. (a) Temperature range between 300K and 1298K (b) Enlargement of temperature range between 300K and 773K. Solid line: mass 28, dash line: mass 44

Comparing CO adsorption amount of all ceria supported catalysts with that of pure ceria in Table 1, CO desorbed from these ceria supported precious metal catalysts is less than expected, as indicated in Figure 28a. This observation reveals not all adsorbed CO was released during the TPD experiment but some remains on the catalyst surface. An oxygen pulse was thus carried out at 1023K for $Pt/CeO_2$ after CO-TPD to look for the missing carbon monoxide, and part of oxygen pulses is shown in Figure29. In addition to some oxygen consumed by the oxidation of ceria, it is found that a great amount of carbon products can still be observed with the introduction of oxygen after previous TPD experiment. This suggests that some of the adsorbed CO on our supported metal catalysts undergoes CO cracking which results in carbon deposition on the metal surface, and hence no expected amount of CO was observed during the TPD.

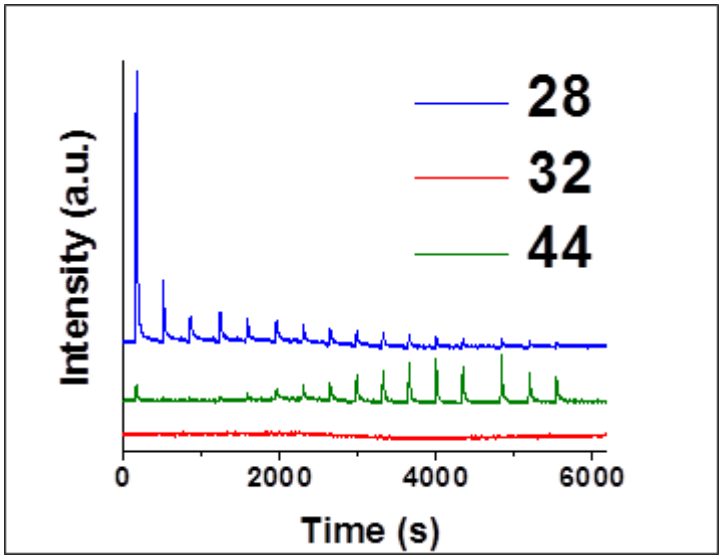


**Figure 29.** Oxygen pulse for 1% $Pt/CeO_2$ at 1023K

In this section, the surface composition was explored. AuPt bimetallic NPs dispersed on both supports all suffered phase segregation after heat treatments and WGS, but all the separated Au still stays on the bimetallic particle surface on the silica. On the other hand, Au atoms were found to be decorated on the surface of Pt-rich particles as ceria was used as support, in addition to some bleeding out of Au NPs as suggested by prior bulk phase studies. This indicates a completely different phase behavior happened to bimetallic NPs spread on different supports. Hence, from the example of immiscible system of Au and Pt, metal-support interactions are critical in the consideration of bimetallic phase behavior and can even dictate catalyst performance in catalytic stability.

# 5.0 CONCLUSIONS

AuPt bimetallic system is one of the combinations of active metals. This bimetallic system is recently intensively studied due to the synergistic effect of AuPt on many reactions. However, like other catalyst systems, the practical applications bimetallic AuPt catalysts rely on not only its catalytic activity but also the high temperature stability. Two objectives were then set for this thesis. Firstly, different from the perfectly miscible system studied by Cao and Veser [41], it is necessary to evaluate if the alloying approach is also applicable to immiscible AuPt. Interestingly, the advantages and disadvantages of each in WGS further motivates the possibility to take bimetallic synergistic effect between Au and Pt through alloying.

In this study, we found that the occurrence of self-stabilization manner for an immiscible combination of Au and Pt strongly depends on the support selected. On the silica, since the low-melting point gold remains in the outer shell as the most stable state after thermal heating, this transition thus could not increase the stability of these AuPt NPs themselves due to the unchanged bimetallic composition. The size distribution thus becomes broad and catalytic reactivity keeps decreasing after thermal treatments. On the other hand, bimetallic AuPt spread on ceria behaves similarly to the previously reported miscible systems, say, low melting point Au diffuses out with elevated temperature and the remaining NPs become more stable up to 700℃ despite of the fact that this segregation started at very low temperature.

Activity and stability for WGS correlate well with the phase behavior of the AuPt bimetallic NPs. The $Au_nPt_{100-n}/CeO_2$ exhibits complete phase segregation prior to the WGS. Accordingly, it performs like a combination of two separated catalysts, bleeding out Au is responsible for the deactivation, while small Pt-rich NPs are stable and shows a bimetallic synergistic effect in WGS reactivity. These Pt-rich NPs also achieve the second goal of this thesis to prepare an alloyed AuPt to improve the stability of Au catalyst. On the other hand, the $SiO_2$ supported bimetallic structure evolves into Pt-rich core/Au-rich shell structure under heat treatments. The surface gold which is not active for WGS thus blocks the active Pt to lower the reactivity of the bimetallic catalyst. This bimetallic catalyst with unchanged composition deactivates over WGS cycles.

Overall, we found that not only the bimetallic compositions but also different support properties like we utilized in this thesis result in a completely different extent of phase segregation. Consequently, combining with the published reports, several factors can be concluded to have great impact on the stability of AuPt bimetallic NPs. These include heat treatment conditions, synthesis methods for AuPt bimetallic NPs, bimetallic compositions, support properties and the loading of bimetallic NPs on supports, which all should be taken into consideration to design an optimal bimetallic AuPt nanocatalyst for realistic applications.

# 6.0 OUTLOOK

Nanoscale structure differs from their bulk counter parts in many significant ways. Bimetallic nanocatalysts are being intensively studied in catalysis [70, 71] in recent years. However, the thermal stability of bimetallic nanoparticles has so far not been given much attention, despite its importance for technical application of nanocatalysts in many industrial high-temperature catalytic processes. Therefore, more research on the correlation between compositions, size and phase behavior of different bimetallic elements in nanoscale is necessary by studying the evolution of single bimetallic nanoparticle as a function of temperature.

In this thesis, we have found that the AuPt bimetallic phase behavior changes with the support properties. The change of bimetallic phases as a function of temperature on silicon dioxide is well understood now. However, due to the extremely small size of the Pt-rich particle on ceria, its exact compositional changes with temperature is not clear. It would be interesting to monitor in situ the changing of these bimetallic particles with temperature via higher resolution instruments, so that we can learn how the bimetallic NPs changes from splitting to fusing and finally to be thermodynamically stable form. Furthermore, although two representative supports were used in this study, it's not enough to give a general conclusion for bimetallic AuPt phase behaviors on all supports. More work should be done for the desired supports in specific applications.

## 6.1 STABILIZATION OF GOLD BY PLATINUM

Because the immiscibility of AuPt, the bimetallic NPs suffer a complete or partial segregation to become a core-shell structure or Pt-rich (Au) particles depending on the support properties and treatment conditions. This self-stabilization method apparently then is not efficient for bimetallic AuPt dispersed on some supports, such as silicon dioxide. Therefore, this approach can also be further combined with the strategy of decoration of thin layer oxide on precious metal catalysts. A promising approach would be to replace $SiO_2$ as with some other functional oxides such as $La_2O_3$ [73, 74], which will make the catalyst a multifunctional one, saving more costs and enhancing its efficiency in reactions.

## 6.2 BIMETALLIC NANOCATALYSTS IN WGS

In terms of the ceria supported AuPt bimetallic catalyst in WGS, this thesis suggests it is potential to replace the more expensive Pt catalyst with this bimetallic catalyst due to the similar activity and good stability. This bimetallic catalyst hence can be considered as a good representative for synergistic effects. However, the bimetallic catalysts used here are made of both noble metals. In order to acquire both economic and high efficiency catalysts in WGS and even other industrial reactions, alloying by replacing one of the noble metals with other cheaper metals could be more beneficial.

# APPENDIX A

## PARAMETERS FOR GC AND CALCULATIONS OF CONVERSION

For this reaction system the inlet concentrations of $H_2$, He, CO are determined by feeding the reaction mixture to the GC directly while bypassing the reactor at room temperature CO conversion in general is defined as

$$X_{CO} = \frac{CO_{in} - CO_{out}}{CO_{in}}$$

The GC used is an Agilent 3000A Micro GC. It is capable of measuring the composition of $CH_4$, $O_2$, $N_2$, $H_2$, CO, $CO_2$, ethane, ethylene, and acetylene. $H_2O$ must be condensed prior to entering the GC system in order to prevent column degradation and inaccurate calculations. The parameters for the GC system are listed in Table 2. Channel 1 (Molecular sieve column) is able to separate $H_2$, He, CO, while channel 2 (Plot U column) is able to analyze $CO_2$.

**Table 2.** GC parameter for WGS

| Parameter | Channel 1 | Channel 2 |
|---|---|---|
| Carrier gas | Argon | He |
| Column type | Molecular Sieve | Plot U |
| Injection type | Backflush | Fixed volume |
| Inlet temperature | 40 ℃ | 40 ℃ |
| Injection temperature | 250 ℃ | 200 ℃ |
| Column temperature | 110 ℃ | 70 ℃ |
| Detector type | TCD | TCD |
| Detector sensitivity | Standard | High |
| Column pressure | 40 psi | 15 psi |
| Post run pressure | 40 psi | 25 psi |
| Backflush time | 9.5 s | --- |
| Sample time | 10 s | 10 s |
| Injection time | 10 ms | 30 ms |
| Run time | 150 s | 120 s |
| Post-run time | 10 s | 60 s |

## BIBLIOGRAPHY


1. L. Mond, C. Langer, British patent, 12608, 1888.

2. K. Kochloefl, G. Ertl, H. Knözinger, J. Weitkamp, hand book of heterogeneous catalysis, 4 Wiley-VCH, Weinheim (1997), 1831.

3. W. Vielstich, A. Lamm, H.A. Gasteiger, Handbook of Fuel Cells: Fundamentals, Technology, and Applications, Wiley, Chichester, 2003.

4. C. Song, Catal. Today 77 (2002) 17–49.

5. S.S. Hla, D. Park, G.J. Duffy, J.H. Edwards, D.G. Roberts, A. Ilyushechkin, L.D. Morpeth, T. Nguyen, Chem. Eng. J. 146 (2009) 148-54.

6. C. Ratnasamy & J.P. Wagner, Catal. Rev. 51 (2009) 325-440.

7. C. Ratnasmy, J.P. Wagner, Catal Rev. – Sci. Eng. 51 (2009) 325-440.

8. L. Lloyd, D.E. Ridler, M.V. Twigg, The water gas shift reaction, Catalyst hand book, 2nd ed, Mansion publishing house, London, 1996.

9. S. Liang, G. Veser. Nanomaterials and energy DOI 10.1680/nme.11.00006 (2011).

10. C. Rhodes, G.J. Hutchings, A.M. Ward, Catal. Today 23 (1995) 43-58.

11. T. Shido, Y. Iwasawa, J. Catal. 141 (1993) 71-81.

12. G.C. Bond and D.T. Thompson, catal. Rev. –sci. Eng. 41 (1999) 319-388.

13. M. Haruta, N. Yamada, T. Kobayahsi and S. Lijima, J. Catal. 115 (1989) 301-309.

14. Y. Wang, S. Lianga, A. Cao, R.L. Thompsona, Götz Veser, Appl. Catal. B 99 (2010) 89–95.

15. D. Andreeva, T. Tabakovaa, V. Idakieva, P. Christova, R. Giovanolib, Appl. Catal. A 169 (1998) 9-14.

16. H. Sakurai, A. Ueda, T. Kobayashi, M. Haruta, Chem. Commun. (1997) 271-272.

17. T. Tabakova, V. Idakiev, D. Andreeva, I. Mitov, Appl. Catalysis A 202 (2000) 91–97.

18. Q. Fu, A. Weber, M. Flytzani-Stephanopoulos, Catal. Lett. 77 (2001) 87-95.

19. A. Sandoval, A. G'omez-Cort'es, R. Zanella, G. D'iaz, J. Saniger, J. Mol. Catal. A: Chem. 278 (2007) 200–208.

20. M. Haruta, Gold Bulletin 37 (2004) 27-36.

21. T. Tabakova, F. Boccuzzi, M. Manzoli, J.W. Sobczak, V. Idakiev, D. Andreeva, Appl. Catal. B: Environmental 49 (2004) 73–81.

22. P. Buffat, J.P. Borel, Phys. Rev. A 13 (1976) 2287- 2298.

23. K. Dick, T. Dhanasekaran, Z. Zhang, D. Meisel, J. Am. Chem. Soc. 124 (2002) 2312-2317.

24. O. Thinon, F. Diehl, P. Avenier, Y. Schuurman, catal. today 137 (2008) 29-35.

25. R. Radhakrishnan, R.R. Willigan, Z. Dardas, T.H. Vanderspurt, AICHE J. 52 (2006) 1888-1894.

26. I.D. González, R.M. Navarro, W. Wenb, N. Marinkovic, J.A. Rodrigue´z, F. Rosa, J.L.G. Fierro, Catal. Today 149 (2010) 372–379.

27. P. Panagiotopoulou, J. Papavasilio, G. Avgouropoulos, T. Ioannides, D.I. Kondarides ,Chem. Eng. J. 134 (2007) 16–22.

28. Y. Zhai, D. Pierre, R. Si, W. Deng, P. Ferrin, A.U. Nilekar, G. Peng, J.A. Herron, D.C. Bell, H. Saltsburg, M. Mavrikakis, M. Flytzani-Stephanopoulos, Science 329 (2010) 1633-1636.

29. P. Panagiotopoulou, D.I. Kondarides, Catal. Today, 112 (2006) 49–54.

30. A. Corma1, P. Atienzar, H. García, J.Y. Chane-Ching, Nature Mater. 3 (2004) 394 - 397.

31. E. Aneggi, J. Llorca, M. Boaro, A. Trovarelli, J. Catal. 234 (2005) 88–95.

32. M. Nolan, G.W. Watson, J. Phys. Chem. B 110 (2006) 16600–16606.

33. Z. Wu, M. Li, S.H. Overbury, J. catal. 285 (2012), 61-73.

34. R. Si, M. Flytzani-Stephanopoulos, Angew. Chem., Int. Ed. 47 (2008) 2884-2887.

35. S. Liang, E. Broitman, Y. Wang, A. Cao, G. Veser, J. Mater. Sci. 46 (2011) 2928–2937.

36. J.M. Zalc, V. Sokolovskii, D.G. L¨offler, J. Catal. 206 (2002) 169-171.

37. Q. Fu, W. Deng, H. Saltsburg, M. Flytzani-Stephanopoulos, Appl. Catal. B 56 (2005) 57-68.

38. M.A. Pablo, C. Massimiliano, S. Ferdi, Angew. Chem. Int. Ed. 118 (2006) 8404-8407.

39. Z. Ma, S. Brown, J.Y. Howe, S. H. Overbury, S. Dai, J. Phys. Chem. C 112 (2008) 9448-9457.

40. M. Cargnello, T. Montin, S. Polizzi, N.L. Wieder, R.J. Gorte, M. Graziani, P. Fornasiero Dalton Trans. 39 (2010) 2122-2127.

41. A. Cao, G. Veser, Nature Mater. 9 (2010) 75-81.

42. A. R. Denton, N. W. Ashcroft, Phys. Rev. A. 43 (1991) 3161–3164.

43. D. Mott, J. Luo, P.N. Njoki, Y. Lin, L. Wang, C. Zhong, Catal. Today, 122 (2007) 378-385.

44. M.L. Wu, D.H. Chen, T.C. Huang, Chem. Mater, 13 (2001) 599-606.

45. M.J. Hostetler, C. Zhong, B.H. Yen, J. Anderegg, S.M. Gross, N.D. Evans, M. Porter, R.W. Murray, J. Am. Chem. Soc. 120 (1998) 9396-9397.

46. J. Luo, M.M. Maye, V. Petkov, N.N. Kariuki, L. Wang, P. Njoki, D. Mott, Y. Lin, C. Zhong. Chem. Mater. 17 (2005) 2086-2091.

47. S. Zhou, G.S. Jackson, B. Eichhorn. Func. Mater. 17 (2007) 3099-3104.

48. P. N. Njoki, J. Luo, L. Wang, M.M. Maye, H. Quaizar, C. Zhong, Langmuir 21 (2005) 1623-1628.

49. B. Zhang, J. Li, Q. Zhong, B. Ren, Z. Tian, S. Zou, Langmuir 16 (2005) 7449–7455.

50. Y. Chen, W.G. Wang, S. Zhou. Mater. lett. 65 (2011) 2649-2651.

51. B.N. Wanjala, J. Luo, R. Loukrakpam, B. Fang, D. Mott, P.N. Njoki, M. Engelhard, H.R. Naslund, J. Wu, L. Wang, O. Malis, C. Zhong, Chem. Mater. 22 (2010) 4282-4294.

52. H.B. Liu, U. Pal, J.A. Ascencio, J. Phys. Chem. C. 112 (2008) 19173-19177.

53. S. Xiao, W. Hu, W. Luo, Y. Wu, X. Li, H. Deng, Eur. Phys. J. B 54 (2006) 479-484.

54. N. Braidy, G.R. Purdy, Gianluigi, A. Botton, Acta Mater. 56 (2008) 5972-5983.

55. A. SaChdev, J. Schwank, J. Catal. 120 (1989) 353-369.

56. O. Malis, M. Radu, D. Mott, B. Wanjala, J. Luo, C. Zhong, Nanotechnology 20 (2009) 1-4.

57. L. P. Singh, S.K. Bhattacharyya, G. Mishra, S. Ahalawat. Appl. Nanosci. 1 (2011) 117-122.

58. Powder Diffraction File (Inorganic Phases); International Center for Diffraction Data: Swarthmore, PA, 1989.

59. M. Hansen, Constitutions of binary alloys, McGraw-Hill, New York, 1958.

60. S.A. Tenney, J.S. Ratliff, C.C. Roberts, W. He, S.C. Ammal, A. Heyden, D.A. Chen. J. Phys. Chem. C 114 (2010) 21652-21663.

61. P. Thormahlen, M. Skoglundh, E. Fridell, B. Andersson. J. Catal. 188 (1999) 300–310.

62. C.S. KO, R.J. Gorte. Surface Science 155 (1985) 296-312.

63. C.R. Henry. Surf. Sci. Rep. 31 (1998) 231-233.

64. B.N. Wanjala, J. Luo, B. Fang, D. Mott, C. Zhong. J. Mater. Chem. 21 (2011) 4012-4020.

65. Z. Yang, T.K. Woo, K. hermansson. Chem. Phys. Lett. 396 (2004) 384-392.

66. M. Nolan, G.W. Watson. J. Phys. Chem. B 110 (2006) 16600-16606.

67. Tana, M. Zhang, J. Li, Y. Li, W. Shen. Catal. Today 148 (2009) 179-183.

68. G.S. Zafiris, R.J. Gorte. Surf. Sci. 276 (1992) 86-94.

69. M. Happel, J. Mysliveček[b], V. Johánek, F. Dvořák, O. Stetsovych, Y. Lykhach, V. Matolín, J. Libuda. J. Catal. 289 (2012) 118-126.

70. W. Hou, N.A. Dehm, R. W.J. Scott, J. Catal. 253 (2008) 22-27.

71. Y. Shen, S. Zhang, H. Li, Y. Ren, H. Liu, Chem. Eur. J. 16 (2010) 16, 7368-7371.

72. S.N. Rashkeev, S. Dai, S.H. Overbury, J. Phys. Chem. C 114 (2010) 2996-3002.

73. H. Zhu, Z. Ma, S.H. Overbury, S. Dai, Catal. Lett. 116 (2007) 128-135.